AN ABSTRACT OF THE THESIS OF

Graysen M. Squeochs for the degree of Master of Science in Water Resources Science presented on April 20, 2011.

Title: Heat Fluxes in the Hyporheic Zone of a Gravel Bar on the Willamette River, Oregon

Abstract approved:

Stephen T. Lancaster Roy D. Haggerty

Increased water temperatures and thermal loading due to anthropogenic inputs has been shown to negatively impact the lifecycles of aquatic organisms in riverine systems (Poole and Berman 2001; Hannah, Malcolm et al. 2004; Quinn, Gagne et al. 2004). The studies enclosed in this thesis evaluate and quantify the heat fluxes within the hyporheic zone of a young unvegetated gravel bar on the Willamette River. The first study evaluated the application of the fiber optic distributed temperature sensing (DTS) system for thermal characterization of the shallow subsurface. The second study utilized data collected via the fiber optic DTS system, combined with data collected by thermistor probes, to calculate an energy balance for the hyporheic zone of the gravel bar. Lessons learned from the first study were that the fiber optic DTS system proved to be a flexible, high data-yielding, temperature monitoring system, but was not without limitations. The system flexibility allowed for the simultaneous

temperature measurement of a 180 m^2 area (river and alcove combined sampling area) and multiple 2 m vertical temperature profiles with vertical resolutions of 0.022 m. Measurements made at the finest resolution of the DTS unit resulted in an increased amount of measurement variability when compared to a more traditional temperature measurement technique. An additional limitation was that the measurement sensor, the fiber optic cable, was inherently very fragile. Our recommendation for future studies is that special considerations must be taken to minimize damage to the fiber cable and signal loss. Nonetheless, the fiber optic DTS system provided an unprecedented view into the shallow subsurface. In the second study, we observed the amplitude of the thermal signal from the river decrease along a hyporheic flow path, while the net hyporheic temperature increased. Contrary to what other studies had found, no hyporheic cooling was observed. Using a simple layer control volume approach, we determined that ground-surface heating was a primary source of heat, via vadose zone storage and transport, for the hyporheic zone. The overlying conclusion of this thesis is that young, unvegetated, gravel bars on the Willamette River similar to the one examined in these studies, may increase the temperature within the hyporheic zone. Therefore, the geometry and the development of vegetation on gravel bars should be considered with regard to river engineering and planning.

Heat Fluxes in the Hyporheic Zone of a Gravel Bar on the Willamette River, Oregon

by

Graysen M. Squeochs

A THESIS

submitted to

Oregon State University

in partial fulfillment of

the requirements for the

degree of

Master of Science

Presented April 20, 2011

Commencement June 2011

Master of Science thesis of Graysen M. Squeochs presented on April 20, 2011.

APPROVED:

Co-Major Professor, representing Water Resources Science

Co-Major Professor, representing Water Resources Science

Director of the Water Resources Graduate Program

Dean of the Graduate School

I understand that my thesis will become part of the permanent collection of Oregon State University libraries. My signature below authorizes release of my thesis to any reader upon request.

Graysen M. Squeochs, Author

ACKNOWLEDGEMENTS

I would like to thank my committee members, Dr. Stephen Lancaster, Dr. Roy Haggerty, and Dr. Mary Santelmann for their encouragement and patience. I would also like to give special thanks to Dr. John Selker and Dr. Anne Trehu. I thank John for his encouragement and assistance with the fiber optic distributed temperature sensing system and HYDRUS software, and Anne for her assistance with the seismic survey deployment and modeling.

This research was funded in part by National Science Foundation grants EAR-0538075 and OCE-0734033. The preliminary study plan for this project was developed by Stephen Lancaster, Roy Haggerty and Anne Trehu.

I would like to give a very special thanks to Michael-David Bushman and Travis Cheney for providing outstanding assistance in the field. Their help was immeasurable.

TABLE OF CONTENTS

LIST OF APPENDICES

LIST OF FIGURES

LIST OF TABLES

LIST OF APPENDIX FIGURES

LIST OF APPENDIX TABLES

DEDICATION

I dedicate this thesis to my family and loved ones. Without their unending love and patience, I would not have endeavored to persevere.

Thank you.

Chapter 1: Introduction

Increased water temperatures and thermal loading due to anthropogenic inputs has been shown to negatively impact the lifecycles of aquatic organisms in riverine systems [*Hannah et al.*, 2004; *Poole and Berman*, 2001; *B Quinn et al.*, 2004]. Within river systems, water temperature regulates fish growth rates, metabolism, migratory patterns and reproduction [*T P Quinn et al.*, 1997]. Additionally, perturbations in thermal regimes can alter the lifecycles of primary producers (e.g. phytoplankton and periphyton) which regulate nutrient cycling and dissolved oxygen concentrations. River temperature also impacts species richness and evenness within a given region.

In accordance with the Clean Water Act, temperature variations are assessed and total maximum daily loads (TMDL) assigned to preserve river systems and ecosystem health. In the Pacific Northwest region of the United States, increased frequency of elevated stream temperature during summer months has continued to impair salmonid viability in many migration corridors. [*National Marine Fisheries Service*, 1999; *B Quinn et al.*, 2004; *Seedang et al.*, 2008] Currently, multiple species of salmonids are endangered and as a result are protected under the Endangered Species Act [USDFW, 2007]. These species require relatively cold water. Increased water temperatures resulting from anthropogenic inputs severely limit the ability of many rivers to provide such habitat [*Harding et al.*, 1998].

The upper Willamette River, OR is one such migratory salmonid corridor where decreased water quality has been a major component in decreasing populations of Chinook salmon and Steelhead trout[*National Marine Fisheries Service*, 1999]. Since stream temperature is the sum of many processes, resource managers are seeking multi-faceted methods to mitigate the current dilemma of elevated river temperatures, and among these methods is augmentation of hyporheic flow through river engineering.

River temperatures are determined by multiple components, which include net insolation (shortwave and longwave radiation), sensible heat flux to and from the air, latent heat flux (evapotranspiration), conduction between the water column and

streambed, and advective heat fluxes to and from adjacent surface and subsurface water bodies [*Evans et al.*, 1998; *Johnson*, 2004]. Processes, such as transient storage or hyporheic exchange zones, may buffer or lag thermal extremes by offsetting and/or minimizing temperature maxima [*Arrigoni et al.*, 2008; *Johnson*, 2004]. The hyporheic zone is defined as a region where surface water that enters the river bed or banks and subsequently reemerges back into the river [*Fernald et al.*, 2006].

Multiple studies of the Willamette River have hypothesized that hyporheic flow may be an important component in the energy balance of the river [*Fernald et al.*, 2001; *Fernald et al.*, 2006; *Seedang et al.*, 2008]. Emergent hyporheic flow has been found to diversify aquatic temperatures by cooling, buffering, and/or lagging [*Arrigoni et al.*, 2008]. The relative impact of hyporheic exchange on stream temperature appears to be proportional to the ratio of hyporheic discharge to main channel discharge. Management schemes for the Willamette River include expectations for hyporheic flow to be a major component of strategies for lowering maximum stream temperatures [USEPA, 2005].

The magnitude of thermal exchange within the hyporheic zone is greatly impacted by the geomorphic history. Morphology, vegetation, and river hydrology all interact in ways that are not readily clear. However, what is clear is that the hyporheic zone can affect the energy regime of a stream. Research has suggested that the hyporheic zone acts as a buffer against large temperature variations on in-stream flow [*Poole and Berman*, 2001], but the mechanics of the buffering capacity is largely unspecified. Therefore, it is unclear as to whether or not increased hyporheic connectivity through gravel inputs will have a significant effect on the mainstem temperature. Additionally, it is unclear as to whether or not surface water is actually cooled by traveling through a hyporheic pathway. There is belief among some that flow through the hyporheic zone could actually cool stream flow although the physics seem to preclude significant cooling of water in the hyporheic zone. Since streams such as the Willamette are used by threatened and endangered species, and engineering solutions to this problem are potentially costly and do not contribute to

ecosystem services, it is important to better understand the heat budget of the hyporheic zone and its effect on steam temperatures.

Therefore, the objective of this study is to identify key thermal inputs and incorporate them into a comprehensive heat balance for a characteristic gravel bar.

The studies enclosed in this thesis evaluate and quantify the heat fluxes within the hyporheic zone of a young unvegetated gravel bar on the Willamette River. The gravel bar was instrumented using sensor arrays which included thermistor probes and two fiber optic distributed temperature sensing probes. The first study evaluated the application of the fiber optic distributed temperature sensing (DTS) system for thermal characterization of the shallow subsurface. The second study utilized data collected via the fiber optic DTS system, combined with data collected by thermistor probes, to calculate an energy balance for part of the hyporheic zone comprising the gravel bar. This thesis will show that young, unvegetated, gravel bars on the Willamette River similar to the one examine in this study may actually increase the temperature within the hyporheic zone. Therefore, the geometry and the development of vegetation on gravel bars should be considered with regard to river engineering and planning.

Chapter 2: Fiber Optic DTS for High Resolution Subsurface Temperature Measurement

2.1 Abstract

Fiber optic distributed temperature sensing (DTS) provides a unique perspective into shallow subsurface profiling. Four fiber optic probes were installed into a gravel bar on the Willamette River, OR to collect temperature data 2 m into the subsurface. Although only two of the four probes successfully recorded data, from the log of the functional probes, we were able to observe the daily heat flux from the surface downward, as well as the fluctuation in the temperature of the hyporheic zone at high resolution without the aid of modeling. We were able to do this because of the measurement flexibility of the DTS system and abundance of data that the system provides. The DTS probes showed that the ground heat flux from daytime insolation penetrated to the water table on hotter days of the recorded period and that there were typically significant heat gradients at or near the water table, but temperature gradients below the water table were generally insignificant.

2.2 Introduction

Subsurface temperature profiling is an environmental sampling technique employed widely in geophysics [*Bach et al.*, 2002] paleoclimatology [*Harris and Chapman*, 1997; *Pollack and Smerdon*, 2004], and hydrology [*Evans et al.*, 1995; *Loheide and Gorelick*, 2006] to evaluate a variety of subsurface physical processes. Under conventional techniques, temperature measurements have been collected using point-oriented logging techniques such as thermistors [e.g.,*Constantz and Thomas*, 1996; *Harris and Chapman*, 2007]

These traditional measurement techniques limited our ability to collect complex multidimensional data sets. In cases where a large number of densely spaced, simultaneous measurements are needed, traditional techniques quickly become cumbersome. Fiber optic distributed temperature sensing (DTS) systems provide a means to integrate spatial and temporal data collection over a wide range of scales. Fiber optic DTS systems have increasingly been used in environmental temperature

sampling, e.g., borehole temperature profiling [*Hurtig et al.*, 1994; *Wisian et al.*, 1998]. Prior applications have used fully extended fiber optic cables, adequate when spatial scales of processes of interest are larger than the sampling resolution of DTS, typically 1 m. However, coiling of fiber optic cables can effectively change sampling resolution from 1 m to less than 0.10 m. For this study we deployed fiber optic DTS probes to capture centimeter-scale subsurface temperature profiles every 5 minutes. This application of the DTS method was used to instrument a gravel bar in the Willamette River, Oregon, to investigate the thermal behavior of hyporheic flow.

2.3 Materials and Methods

2.3.1 Site Description

The Willamette River basin has a drainage area of 29,728 km^2 and a length of 424 km. The majority of the groundwater in the Willamette Valley is contained in a 500 m thick Neogene and Quaternary alluvial fill aquifer. The lower 400 m is composed of fine-grained Mio-Pliocene fluvial-lacustrine sediments, while the upper 100 m consists of multiple coarse-grained Quaternary age deposits. The southern portion of the Willamette Valley, including the study site, consists of five Quaternary units. The upper two are located in the central area of the valley. The units, Holocene silts and sands (0–10 m depth) are underlain by late Pleistocene sand and gravel deposits (5–15 m depth). These central valley units are bound by two early-mid Pleistocene deposits to the east and west. The upper, a mid-Pleistocene deposit, consists of Missoula flood clays, silts and sands (0–10 m depth). The lower, an early Pliocene deposit is Willamette river sand and gravel sediments (10–20 m depth). These are all underlain by Tertiary weathered gravels (20–100 m depth).

The gravel bar chosen for this investigation is located on the western side (river-left) at river km 261 (44°15’35.8” N, 123°10’30.5”W) (Figure 2.1). The gravel bar first appeared in 2005 and accreted annually until this investigation in the summer of 2007. During the dry season (June to September), the water surface on the river-left side of the bar was connected to the mainstem only at the downstream end of the bar, so that the bar formed an alcove [*Fernald et al.*, 2001]. Throughout the dry period, the

adjacent alcove had an average depth of 0.75 m and covered an area of approximately 360 m^2. Vegetation on the bar was primarily limited to small forbs[1] and young woody plant species[2]. The bar surface was comprised of poorly-sorted gravels (median particle diameter, D_{50} = 0.032 m; D_{10} = 0.011 m, and D_{90} = 0.070 m). The site was part of an island bounded on the river-right and –left by the mainstem and a side channel, respectively, and thus was accessible only by boat.

2.3.2 Instrumentation

An Agilent N4386A DTS unit (Santa Clara, CA, USA) with a Fujitsu Stylistic ST1000 tablet PC (Tokyo, Japan) was deployed for onsite configuration and data storage. Using time-domain reflectometry, laser light is pulsed into the optic cable, and a fraction of the light is scattered and reflected. A portion of the backscattered light is shifted to coherent side-bands at wavelengths longer and shorter than that of the incident light. The ratio of the temperature independent Stokes side-band (shorter wavelength) to temperature sensitive Anti-Stokes side-band (longer wavelength side-band) scattering provides temperature information and timing of return signals provides spatial location [*Selker et al.*, 2006; *Tyler et al.*, 2009].

We used two duplex (i.e., double-stranded), multimode Kaiphone fiber optic cables (Taipei, Taiwan). The first was armored (wrapped with stainless steel strands and sheathed in an additional polyethylene cover, outer dia. 3 mm). The second cable was not armored (comprised of two strands of optical fiber inside a plastic sleeve, outer dia. 3 mm). The armored cable was used to monitor the ground surface temperature. The non-armored cable was used in the fiber optic probes to monitor temperature within the gravel bar. Both cables were connected to the DTS unit with APC e2000 fiber optic connectors and a fiber optic fusion welder. The duplex cables

[1] Examples: Senecio vulgaris (common groundsel), Rumex crispus (curly dock).

[2] Example: Salix mackenzieana (Mackenzie willow), Populus trichocarpa (Black Cottonwood).

allowed for a double-ended measurement scheme so light attenuation along the cable could be automatically calibrated [*Tufillaro et al.*, 2007].

Six fiber optic probes were constructed from 2.0 m lengths of 0.064 m diameter, schedule 80, PVC pipe. PVC pipes were threaded end-to-end to within 0.10 m of both ends with a steel lathe. Thread spacing was 3 threads per centimeter and the thread depth was 1.5 mm. Eighty meters of unarmored cable was wound into the threads of each probe by lathe. The ends of the fiber optic cable were routed through the center of the pipe via slots cut at the top and the bottom. In this way, the 80 m length of fiber optic cable was condensed into a 1.80 m interval. Sampling at 1.0 m intervals along the cable (the minimum spatial resolution of the DTS unit) yielded a 0.023 m vertical resolution along the probe.

Four fiber optic probes were installed in the gravel bar. Their orientations were intended to parallel the dominant subsurface flow direction across the gravel bar. The water table map used for preliminary probe placement was constructed by measuring water surface elevations from around the perimeter of the gravel bar and alcove. The water surface elevation measurements were made using a total-station[3]. The technique of probe installation was a modified version of the direct-push method for monitoring well installation in near surface aquifers. In this case, a 76 mm steel sleeve was slid over a 65 mm steel driving rod. The sleeve and driving rod were simultaneously driven into the gravel using a hand operated pile driver. Once 2 m depth was reached, the driving rod was removed from the steel sleeve and a fiber optic probe was inserted in place of the driving rod. The steel sleeve was then removed to allow the gravel to settle and come into contact with the fiber optic probe.

The fiber optic cable attached to the DTS unit was divided into five sections. The first section comprised the armored duplex cable. This section extended from the

---

[3] A total station is a surveying instrument which is the combination of an electronic transit and an electronic distance meter (EDM). It is used to measure and record points in space.

DTS unit into the alcove, across the surface of the gravel bar, and into the river. In the alcove and river, the cable was laid in a three span serpentine configuration. The spans were centered on the fiber optic probe array, and each span was 30 m in length with a 1 m separation between spans (Figure 2.1). The cable was secured to the bed of the alcove and river using steel rebar driven into the bed sediments as anchors for the turns and occasionally placing, approximately 0.2 m diameter, stones on the cable for the duration of the experiment. The fiber optic cable was attached to the anchors via a length of small diameter nylon rope and wedge clamps were used so that cable was not stressed in the turns.

The remaining four sections of fiber optic cable were lengths of non-armored cable wound onto the PVC probes. The fiber optic probes were installed A, B, C, D, with probe A closest to the river and probe D closest to the alcove. Of the four probes installed at the site, only two, B and C, were successfully fused in sequence and connected to the first (armored cable) section. Several attempts to fuse probes A and D into the sequence were made, but were unsuccessful due to a malfunctioning fusion welder.

The DTS system was calibrated by adjusting three variables: the attenuation ratio, offset, and gain. Attenuation ratio corrects for signal loss along the fiber optic cable. Offset and gain corrections adjust the difference and amplification, respectively, between the raw temperature trace produced by the DTS unit and a real temperature value.

As outlined in the manufacturer's calibration literature [*Agilent Technologies*, 2007], the offset correction was calculated by comparing the raw temperature trace recorded by the DTS and measurements made in an ice bath. Gain was determined by comparing the temperatures recorded in the ice bath with those recorded at another location on the cable. The ice bath consisted of an ice slurry in a 66 L insulated container. The temperature of the bath was recorded several times throughout the experiment with a precision VWR digital thermometer with a resolution of 0.001° C and an accuracy of ±0.05° C. An Onset Tidbit V2 temperature data logger (0.02° C

resolution and ±0.2° C accuracy) [Bourne, MA, USA] was secured to the central point of the river section and provided the additional monitoring point for the gain adjustment.

2.4 Results

Temperatures were recorded from September 7, 2007, to September 12, 2007, at a sampling interval of 5 minutes, from probes B and C, the river, alcove, and across the surface of the gravel bar (Figure 2.2; the gravel bar surface temperature record was omitted from the figure for clarity). The river and alcove traces are less dynamic than the fiber optic probe traces because they represent the average of each serpentine configuration, each covering 90 m^2 of bed surface. For complete data series, see "Fiber Optic DTS Data" folder in attached CD.

Probe traces reveal the flux of heat from the surface downward into the gravel bar (vertical axis) over time (horizontal axis) and provide a basis for estimating heating front propagation rates. Examining a single heating episode (1 day- 9/9/07), we detected that the heating front propagated downward from the surface at varying rates. There were three distinct regions. In the first region (0.00–0.05 m depth), the heating front propagated faster than the DTS sampling period (5 minutes). This indicated a heat propagation rate greater than 0.60 m hr^{-1}. The time required for the heating front to propagate over the second region (0.05–0.40 m depth) was 4 hours. This was equivalent to a propagation rate of 0.09 m hr^{-1}. The heating front took 6 hours to cross the third region (.40 –0.45 m depth). This was equivalent to a propagation rate of 0.008 m hr^{-1}

Beyond 0.45 m depth, an abrupt change occurred in the heating front propagation. This change in behavior marked the interface of the unsaturated zone with the saturated zone. The saturated zone exhibited a different behavior than the unsaturated zone. The average temperature for the measurement period of region 3 was 19.4 °C. The average temperature of the unsaturated zone over the sampling period was 18.5 °C. The unsaturated zone was consistently 0.9 °C warmer than the

saturated zone. This difference indicated that thermal exchange was likely occurring at the unsaturated/saturated zone interface.

After the calibration factors were applied, the DTS River temperature record was compared to the Tidbit V2 temperature record. The root mean squared error between the DTS and the Tidbit V2 was ±0.3 °C.

2.5 Discussion and Conclusions

Assuming media properties remained constant over the length of the probe, the change of the heating front propagation rate over the 3 regions along the profiles suggested a change in transport processes. Logical inference suggests that the change in transport processes was predominately governed by water content, save for region 1. Region 1 was assumed to be the result of heating from solar radiation. Region 2 may have been due to convective air exchange, and region 3 was likely the result of conductive exchange. Region 2, where air filled pores were continuous, air convection could move heat downward relatively quickly; below the water table, where water filled pores are continuous, the temperature profile indicated well-mixed conditions; region 3, where air and water-filled spaces were both discontinuous in the capillary fringe, heat flow is limited by conduction and is therefore relatively slow. This suggests that the capillary fringe acted as an insulator for the saturated zone and limited the ground heat flux from the surface to the water table, where air convection could have otherwise led to rapid heating from the ground heat flux.

The similarity between the fiber optic probe saturated zone temperatures traces presented in Figure 2.3 is of significant interest. We see that the arrival time of the peak temperature for each probe was nearly identical, but the temperatures are offset. Previous research on hyporheic flow suggests that the arrival times of peak temperatures along hyporheic pathways become increasingly lagged [*Arrigoni et al.*, 2008].

The absence of an offset in the arrival time of daily maximum temperature in our findings suggest that our probes were not oriented along a singular hyporheic pathway, rather, the probes sampled parallel hyporheic pathways. Therefore, it is

plausible that our initial estimates of the direction of hyporheic flow through the gravel bar were incorrect. To correct for this, additional analysis (i.e., numerical ground water models, ground water tracer tests) should be performed to verify this conclusion. The offset in temperature between the probes may be attributed to the depth of gravel above the water's surface. Therefore, the greater temperature recorded by probe B may likely be due to the insulative properties of sediment depth.

Fiber optic probes A and D were unusable. The reason for this is unclear. One possibility is that the probes could have become damaged during the installation process. The design of the fiber optic probes left the sensitive cable exposed to the elements. If a sharp edge came in contact with the cable at any point during the installation, it is likely that the cable could have been severed. Another possibility is that the fusion joint application in the field was unsuccessful, exposing one limitation of the DTS system. Since the sensor medium is a small glass fiber (0.9 mm), its inherent fragility can make fusions in the field difficult. Too small of turn radii and kinking proved to be two major problems that must also be avoided in order to prevent signal loss or signal breaks.

An important feature that sets fiber optic DTS apart from point sampling methods is the dependence of measurement accuracy on the spacing of measurement zones along the fiber and the number of measurements taken at each zone. With fiber optic DTS, the reported measurement is the average of multiple measurements taken within the time sampling interval. Thus, longer time sampling intervals result in a greater number of measurements averaged per reported value. Additionally, the larger the zone of integration, the greater the return signal for measurement. Because the rates and zones of temperature change for the gravel bar were not well known, we used the highest DTS resolution allowable (1 m spacing of sampling points and an interval of 5 minutes was chosen). As a result, a higher degree of variability in the reported temperatures was observed when the fiber optic DTS data was compared to the more traditional thermistor collected data. A comparison of the fiber optic DTS

data and V2 Tidbit data can be seen in Figure 2.4. The V2 tidbit was attached to the shielded fiber optic cable in the river.

Spatial variability can be problematic for discrete point sampling methods. With the fiber optic DTS methods detailed here, multiple spatial and temporal scales can be efficiently sampled simultaneously by expanding or contracting the orientation of the fiber optic cable. Ultimately, point measurements are appropriate when the domain of measurement is homogeneous. However, homogeneous conditions are not a common condition in natural settings. The simplest method to address heterogeneities is to increase the number of sampling points. The ability to increase the number of sampling points in continuous sequence through heterogeneous substrates is one of the largest benefits of DTS technique. The continuity of the fiber optic cable effectively provides discrete, densely spaced measurements, which aids in the reduction of assumptions associated with heterogeneity.

In closing, the fiber optic DTS system proved to be a flexible, high data-yielding, temperature monitoring system. The system flexibility allowed for the simultaneous temperature measurement of a 180 m^2 area (river and alcove combined sampling area) and multiple 2 m vertical temperature profiles with vertical resolutions of 0.022 m. Because of the fine resolution of the temperature profiles, we were able to observe subtle changes in the propagation rate of heat in the unsaturated zone of a gravel bar on the Willamette River and delineate the interface between the unsaturated and saturated zone. We observed a significant ground heat flux reaching the saturated zone from radiation at the surface, but only on certain days. The heat from the surface propagated relatively quickly to depths approximately 5 cm above the water table but much more slowly within 5 cm of the water table, and temperatures below the water table were nearly uniform. While the fiber optic DTS system is a very versatile tool, the system is not without limitations. Sampling at the finest resolution of the DTS unit resulted in an increased amount of measurement variability when compared to a more traditional temperature measurement technique. An additional limitation is that the measurement sensor, the fiber optic cable, is inherently very fragile and special

considerations must be taken to minimize signal loss. Nonetheless, the fiber optic DTS system provided an unprecedented view into the shallow subsurface.

2.6 Figures

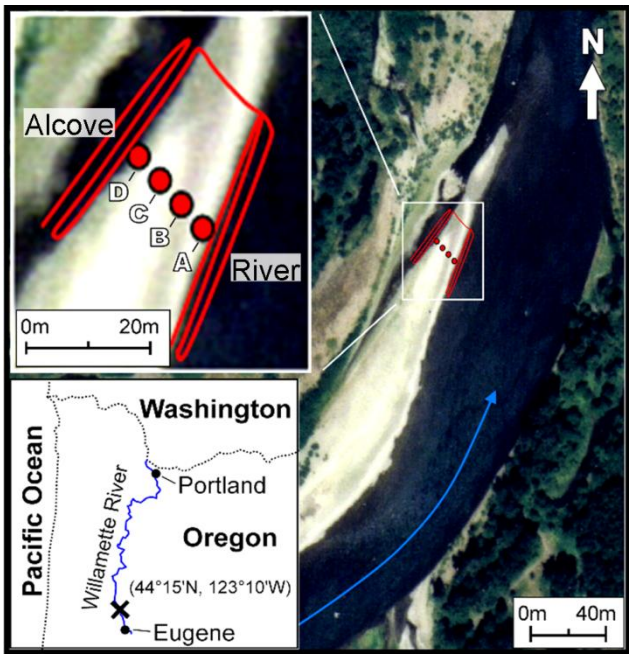

Figure 2.1 Study site location and instrumentation layout

The site is located on the Willamette River at river km 261. The inset image at the top left contains the layout of the fiber optic instrumentation. The armored cable is laid out in two serpentine configurations, beginning in the alcove then spanning across the surface of the gravel bar and ending in the river. The fiber optic probes are labeled A–D.

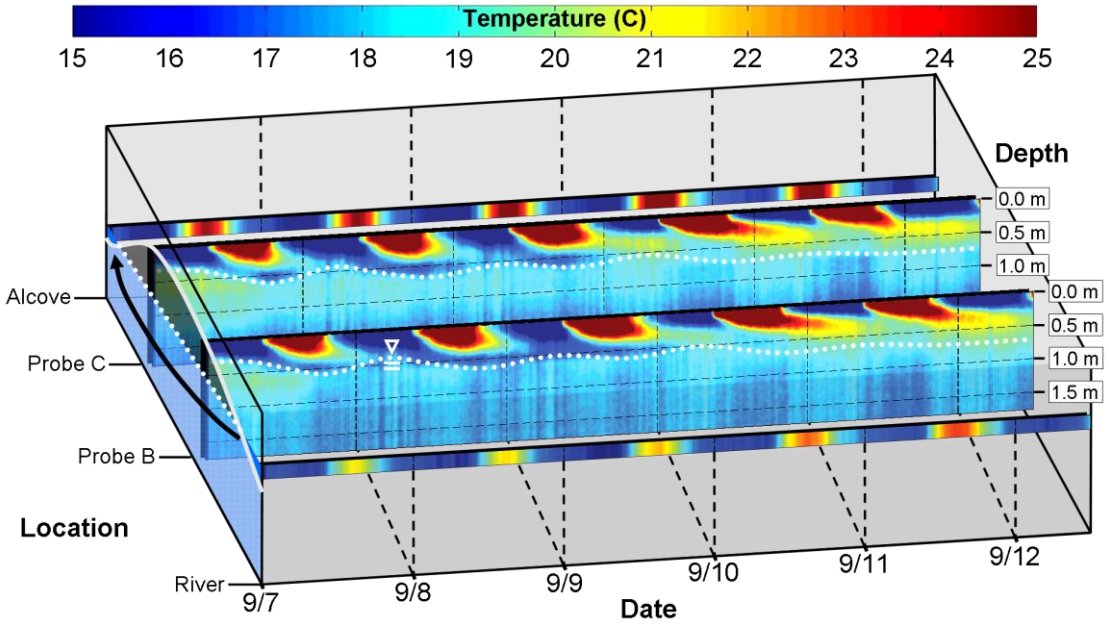

Figure 2.2 Fiber Optic distributed temperature sensing (DTS) data summary

This is the summary of the fiber optic DTS data collected at the site (the surface temperature of the gravel bar was omitted for reasons of clarity). Each time series trace in Figure 2 is arranged according to their orientation on the gravel bar (see Figure 1). The river and alcove temperature traces represent the averages from their respective configurations. The dotted lines on the probe traces represent the variation in the water table over the sampling period. The daily heat flux from the surface can readily be seen as well as the fluctuation of the temperature in the hyporheic zone.

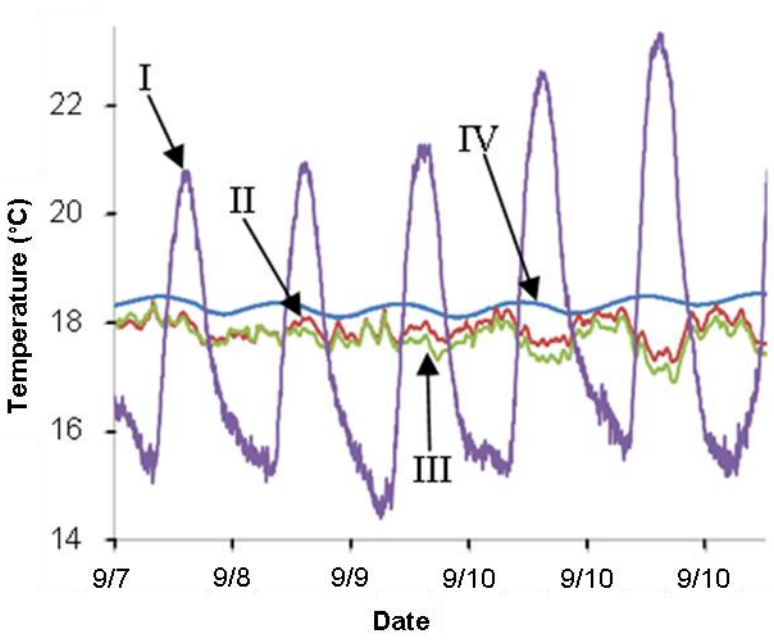

Figure 2.3 Comparison of fiber optic probe hyporheic zone measurements

A comparison of the fiber optic DTS measurement (I–III) and a V2 Tidbit temperature logger (IV). The River (I), Probe B (II), and Probe C (III) reveal the separation in the lag in the arrival of the peak daily temperature for each location. Traces (II) and (III) represent the averages from the lower sections of the probes (1.30–1.70 m depth). Trace (IV) is the record from a point 5 m north of probe B. Trace (IV) is from 1.10 m depth. Comparing the DTS traces to the Tidbit, the variation generated by the DTS unit is readily apparent.

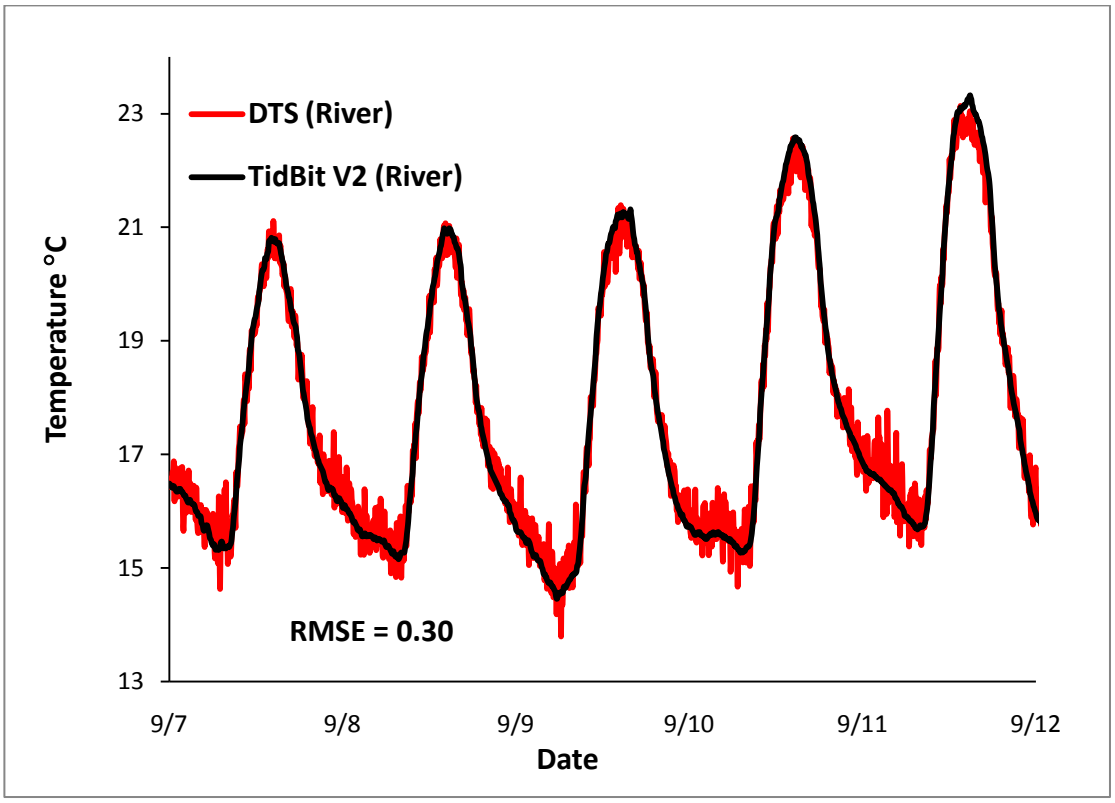

Figure 2.4 Comparison of fiber optic DTS data to V2 Tidbit data

Comparison of the fiber optic DTS (red) to a V2 Tidbit Thermistor (black). The Tidbit was secured to river section of the fiber optic cable. Comparing the two datasets the root mean squared difference was ±0.3 °C.

Chapter 3: Heat Fluxes in the Hyporheic Zone of a Gravel Bar on the Willamette River, Oregon, USA.

3.1 Introduction

Increased water temperatures and thermal loading have long been shown to negatively impact the lifecycles of numerous aquatic organisms in riverine systems [*Hannah et al.*, 2004; *Poole and Berman*, 2001]. In the Pacific Northwest region of the United States, the increased frequency of elevated stream temperature during summer months for the last few decades has increasingly impaired salmonid viability in many migration corridors [*Geist et al.*, 2002; *National Marine Fisheries Service*, 1999; *B Quinn et al.*, 2004; *Seedang et al.*, 2008]

The thermal energy balance for stream systems is controlled by several processes. The external processes are: solar radiation (shortwave radiation), shading, air temperature (longwave radiation), wind speed and groundwater inputs [*Evans et al.*, 1998; *Johnson*, 2004]. Internal processes, such as transient storage or hyporheic exchange zones, may buffer or lag thermal extremes by offsetting and/or minimizing temperature peaks [*Arrigoni et al.*, 2008; *Johnson*, 2004].

Hyporheic exchange has several operative definitions; however, we define it as surface water that enters the river bed or banks and reemerges back into the river [*Fernald and Guldan*, 2006]. Until recently, the impact of these transient flow regimes on stream temperature has been thought to be minimal; however, more recent studies have suggested hyporheic exchange may be a more significant component of the stream energy balance [*Arrigoni et al.*, 2008; *Johnson*, 2004; *Loheide and Gorelick*, 2006; *Story et al.*, 2003].

The impact of hyporheic exchange on stream temperature is largely governed by the geomorphic history and flow regime of the river system. Studies of low order streams by Johnson [2004] and Loheide and Gorelick [2006] found transient flow to alter stream temperature at the reach scale; whereas studies of higher order streams concluded that hyporheic discharge [*Burkholder et al.*, 2008; *Fernald et al.*, 2006] had minimal impact on mainstem temperature but may have increased thermal

heterogeneity in the stream system. Thermal heterogeneities manifest as localized cool zones or temperature anomalies, such as those observed by Burkholder et al. [2008]. These anomalies are likely the result of transport processes (advection and dispersion plus additional sources or sinks) "cooling, buffering, and/or lagging" the temperature of water flowing through the hyporheic zone [*Arrigoni et al.*, 2008].

The transport processes of advection and dispersion, in conjunction with physical processes of bed conduction, and atmospheric contributions of latent and sensible heat, contribute to temperature signatures of water within the hyporheic zone [*Evans et al.*, 1998]. However, prior studies have found advective transport to be the dominant process [*Keery et al.*, 2007; *Silliman and Booth*, 1993; *Silliman et al.*, 1995; *Stallman*, 1965]. As summarized in Arrigoni et al. [2008], multiple studies have found seemingly conflicting information regarding the role of the hyporheic zone with respect to the impact of hyporheic exchange on stream temperature [*Arrigoni et al.*, 2008; *Fernald et al.*, 2006].

The upper Willamette River, Oregon is a major salmonid migratory corridor where decreased water quality, specifically increased water temperature, has led to decreasing populations of Chinook salmon and Steelhead trout [*Laenen and Dunnette*, 1997]. Stream temperature is the sum of many processes; as a result, resource managers are seeking multi-faceted methods to mitigate the current dilemma of elevated river temperatures. Multiple studies [*Fernald et al.*, 2001; *Fernald et al.*, 2006; *Seedang et al.*, 2008] of the Willamette River have hypothesized that thermal pollution may be decreased by transient flow regimes but there have been few comprehensive studies examining the thermal energy balance of hyporheic water and the potential impact on mainstream temperature. Gravel augmentation is being considered as a potential method to increase hyporheic connectivity and possibly buffer daily maximum temperatures. Currently, regulators are investing significant resources to increase hyporheic flow as a means to mitigate thermal pollution.

Thus, our study was motivated by the need to understand if and how the energy content of stream water could potentially be lowered by flowing through the hyporheic

zone. The objective of our study was to identify key thermal parameters and develop a comprehensive heat balance for a characteristic gravel bar. By employing high resolution data collection systems to a well-characterized gravel bar in the mainstream Willamette River, OR we were able to quantify thermal inputs to hyporheic water for the study area. The software packages Groundwater Modeling System (GMS) 6.0 and HYDRUS 3D were used to determine hyporheic flow geometry and estimate the thermal properties of the gravel bar. Using an energy balance, we quantified the dominant thermal fluxes within the hyporheic zone. For a young, sparsely vegetated gravel bar, we observed a net increase in energy content due to surface heating over the length of study.

3.2 Materials and Methods

3.2.1 Site Description

3.2.1.1 The Willamette Drainage/Valley Floor

The Willamette River drainage is a 29,728 km^2 area in western Oregon, USA. The Cascade Mountain Range forms the eastern boundary of the drainage, and the Oregon Coast Range forms the western boundary. The floor of the Willamette Valley is comprised of a 500 m thick Neogene and Quaternary alluvial fill aquifer. The lower 400 m is composed of fine grained Mio-Pliocene fluvial-lacustrine sediments, while the upper 100 m consists of multiple coarse-grained Quaternary age deposits. The southern portion, or upper Willamette Valley, consists of five Quaternary units. The upper two are located in the central region of the valley. They are Holocene silts and sands (0–10 m depth) underlain by late Pleistocene sand and gravel deposits (5–15 m depth). These central valley units are bound on the east and the west by two early-mid Pleistocene units. The upper of these deposits, a mid-Pleistocene unit, consists of Missoula flood clays, silts, and sands (0–10 m depth), while the lower early Pliocene deposit is Willamette River sand and gravel sediments (10–20 m depth). These are all underlain by Tertiary weathered gravels (20–100 m depth) [*O'Conner et al.*, 2001].

3.2.1.2 The Willamette River

The Willamette River is a 424 km, 8th order, predominately anastomosing alluvial stream. The mainstem of the Willamette River begins at the confluence of the Coast Fork and Middle Fork of the Willamette at the southern end of the Willamette Valley. The river then flows northward approximately 300 km and terminates at the confluence with the Columbia River. The climate of the Willamette Valley is classified as Mediterranean. The valley typically experiences cool, wet winters and warm, dry summers. The average precipitation is approximately 120 cm per year [*Oregon Climate Service*, 2007]. Peak annual discharge typically occurs between the months of November and March as a result of winter and spring precipitation. For the remainder of the year, discharge is primarily governed by upstream reservoir operations. The average annual discharge at river km 260 is 328 m^3 $second^{-1}$. Between the months of July–September 2007, the average monthly discharge was 126 m^3/second [*Harrisburg USGS Gauge 14166000*, 2007]

The predominant natural bank materials of the modern upper Willamette River are Holocene gravels and Indurated Pleistocene gravels. Of these two, the Holocene gravels are the more erodible and are the primary source of sediment input for the formation of new geomorphic features such as gravel bars [*Wallick et al.*, 2006]. Gravel bar formation is normally the result of lateral migration of meander bends. Sediment eroded from the outer bank is transported longitudinally downstream, forming either mid-channel or lateral gravel bars. As erosion progresses and more sediment is input into the stream, the mid-channel or lateral bars aggrade and can sometimes develop into point bars if the sediment input is large enough. Young point bars are typically cross channel bars that are inundated during peak flows, but become point bars during the low flow season, i.e., summer months. At these times, water ceases to flow over the head of the bar and an alcove will form on the side opposite the river.

3.2.1.3 The Research Site

The point bar chosen for this investigation is located on the western side (river-left) at river km 261 (44°15'35.8" N, 123°10'30.5"W) [Figure 3.1]. The site was accessible only by boat. The first appearance of the gravel bar was in 2005. The gravel bar accreted annually until the time of this investigation in the summer of 2007. During the dry season (June to September), the water surface on the river-left side of the bar was connected to the mainstem only at the downstream end of the bar, so that the bar formed an alcove. Throughout the dry period, the adjacent alcove had an average depth of 0.75 m and covered an area of approximately 360 m^2. Vegetation on the bar was limited to small annual forbs. The bar surface was comprised of poorly-sorted, mildly imbricated gravels (median particle diameter, D_{50} = 0.032 m; D_{10} = 0.011 m, and D_{90} = 0.070 m).

3.2.2 Measurements/Instrumentation

3.2.2.1 Surveys

We conducted three surveys to map the physical structure of the site: topographic, bathymetric, and seismic. The topographic mapping of the gravel bar and its surrounding area was performed through the combination of total station[4] and precision GPS[5] data. The alcove and bar surface were mapped at approximately a 2 m interval. The area surrounding the bar was mapped at an approximate interval of 3 m. The bathymetric survey was performed with the use of a nautical GPS[6] system that had the capability to record both horizontal position and depth. The river channel was mapped at an approximate 3 m interval. Subsurface structure was determined using a seismic survey method. Using a 60 channel linear geophone array, two seismic

---

[4] Leica TCM-1100- electronic transit and electronic distance meter (EDM) with data storage capability. Manufacturer Stated accuracy: ±0.01 m vertically and horizontally at 1000 m distance.

[5] Trimble Pathfinder- Using maximum resolution settings with radio telemetry correction, the accuracy is stated as ±0.05 m.

[6] Garmin GPSMAP® 185 Sounder- Manufacturer Stated Accuracy: Horizontal ±1–5 m; Depth ±0.10 m.

surveys were conducted. The first was oriented on the longitudinal center line of the gravel bar with a geophone spacing of 2.5 m. The second survey ran orthogonally to the centerline and transected the bar at the midpoint. The geophone spacing for the transverse seismic survey was spaced at a 2 m interval. A more detailed description the survey methods and procedures are located in the appendix (appendices: A-1 Topographic Survey, A-2 Bathymetric Survey, and A-3 Seismic Survey).

3.2.2.2 Temperature Data

3.2.2.2.1 Fiber Optic Distributed Temperature Sensing

A fiber optic distributed temperature sensing (DTS) system was deployed as described in the prior chapter. Four 2 m PVC pipes wrapped in fiber optic cable were installed into the bar and 180 m of fiber optic cable was collectively deployed in the river and alcove. The DTS system was configured to record a temperature data point for every meter of cable every 5 minutes. By wrapping the fiber optic cable onto a 0.064 m diameter threaded PVC pipe, the 1 m spacing between data points was condensed to an interval of 0.025 m.

3.2.2.2.2 Thermistor Probes

In addition to the fiber optic DTS system, temperature was collected using Onset Tidbit V2 Temperature Data Loggers[7]. The V2 loggers were attached to a 3.8 cm PVC rod and inserted into larger (7.62 cm) PVC pipe which had a slot cut into the side of it to allow the V2 loggers be directly exposed to the gravel in the hyporheic zone. In this configuration, the V2 loggers were dubbed "thermistor probes." Each thermistor probe housed 5 V2 loggers spaced at a 10 cm interval. The thermistor probes were deployed in an orientation that paralleled the fiber optic probe array (see Figure 1). The top V2 logger on each probe was positioned approximately 1–2 cm

[7] Onset Tidbit V2 Temperature Data Loggers- Manufacturer Stated Accuracy: Resolution 0.02° C and an accuracy ±0.2° C.

below the water's surface inside each probe casing. An air bladder was then inflated inside the probe's casing to extrude the loggers into the gravel (see Appendix D).

3.2.2.3 Piezometer Array

A piezometer array was installed so that groundwater elevations could be monitored and aquifer characterization tests could be performed. The piezometers were constructed from 0.032 m diameter PVC pipes, and were installed using a modified form of the direct push method. The method is similar to that used to install the fiber optic and thermistor temperature probes. The aquifer characterization tests included slug/falling head hydraulic conductivity tests and salt tracer injection/recovery tests. Auxiliary temperature measurements were also recorded using the piezometer array.

3.2.3.4 Hyporheic and Heat Flux Simulation

3.2.2.3.1 Hyporheic Flux/Flow Geometry Simulation

A three-dimensional, steady-state ground water flow model was created to simulate hyporheic flow through the gravel bar. The flow model was developed via the Groundwater Modeling Systems (GMS) 6.0 software platform, utilizing the MODFLOW [*McDonald and Harbaugh*, 1988] and MODPATH modules.

Using survey, piezometer, and aerial photography data, a 40 layer finite-difference grid frame was created using the conceptual model approach. The grid size ranged from 0.20 m X 0.20 m X 0.20 m (X, Y, and Z planes respectively) in the area of the instrumentation to 5 m X 5 m X 2 m (X, Y, and Z, respectively) at the outer boundary. The outer boundary condition was set as a no flux boundary. River stage elevation was characterized as a specified head boundary condition, and the stage elevation remained constant throughout the simulation. Once a successful MODFLOW simulation was generated, the MODPATH module in GMS was used to simulate hyporheic flow paths and determine flow geometry through the bar. Additionally, the particle tracking feature of MODPATH was used to calibrate the model by matching particle arrival times at the well locations with the arrival times of

a peak temperature markers in hyporheic flow. A more detailed description of the model construction is located in the appendix (see Appendix F: Groundwater Model).

3.2.2.3.2 Heat Flux Simulation

A two-dimensional finite element transient heat transport model was created using HYDRUS 3D [*Šimůnek et al.*, 2005]. The domain dimensions of the heat transport model were taken from a cross-sectional slice in the XZ plane (parallel to flow lines) of the GMS groundwater model at the location of the instrumentation. The finite element grid size ranged from a value of 0.2–2.0 m. Nodal spacing was refined to 0.2 m in the zone where field measurements were made, and the left, right, and bottom boundaries were set at a 2 m nodal spacing. The boundary conditions for fluid flow were constant throughout the simulation, while the boundary conditions for heat transport were imported values from field observations. (See Appendix G: Heat Model). Additionally, a sensitivity analysis of the temperature transport model was performed. Two scenarios were simulated. In the first scenario, the gravel bar surface temperature was held constant at the weekly average. This scenario was created to estimate the influence of diurnal surface heating on hyporheic temperature. In the second, a cooler region was created in the lower portion of the model domain. This scenario was created in order to simulate hyporheic flow mixing with a cooler, deeper aquifer and estimate the degree of influence mixing with deeper aquifers might have on hyporheic temperature.

3.3 Results

3.3.1 Temperature Data

3.3.1.1 Distributed Temperature Sensing (DTS) Data

Temperature data were collected to constrain the initial and boundary conditions for numerical simulations of advective (hyporheic) heat transport in the gravel bar and to provide calibration data. The high density of data points in the fiber optic DTS dataset provided a high resolution visualization of heat transport within the aquifer. Figure 3.2 illustrates the summary of the fiber optic DTS dataset. The horizontal positions of the four measurement locations are plotted: the river, probe B,

probe C, and the alcove. Examination of the fiber optic probe profiles reveals two dominant temperature signals. The first signal is the temperature fluctuation associated with the propagation of heat from the surface downward into the vadose zone. The second is the temperature signal of the advecting (hyporheic) water. The fluctuation in temperature from the surface signal has a larger amplitude (30 °C) than that of the hyporheic water amplitude (0.5°C). The hyporheic water is out of phase -11 hours later, indicating that the signal lags behind the surface phase 11 hours. For the first three days of the sampling period (9/7–9/10), an abrupt temperature transition occurred at the water table. The transition became less distinct for the final two days. The average amplitude of the daily oscillation in river stage was 0.005 m. River stage elevation dropped 0.025 m over the sampling interval.

3.3.1.2 Thermistor Data

The thermistor temperature data were collected to support the fiber optic DTS data as well as for use in calibration of the numerical simulation of heat transport. Figure 3.3 presents the summary of the thermistor data from row 3 collected for dates 9/7–9/21. Due to a failure in fiber optic probes A and D, temperature behavior was not monitored in the direction of hyporheic flow across the gravel bar using the fiber optic DTS system. However, the thermistor probe row (row 3) adjacent to the fiber optic probe row (row 2) successfully captured the temperature parallel to hyporheic flow across the gravel bar (see instrumentation inset from Figure 3.1). Temperature traces from probes represent temperature 10 cm (±3 cm) below the water table. Attenuation of the diurnal temperature signal as it travels across the hyporheic aquifer can be observed in Figure 3.3. The river temperature amplitude ranges from 10–2 °C with a period of 24 hours. The daily average temperature of the river was plotted to reveal a local maximum temperature over the sampling interval. This local maximum was observed propagating across the gravel bar. With t = 0 hours when the average daily maximum temperature was reached, the maximum arrived 6.83 hours at the first probe (3A). 18.66 hours from t = 0, the maximum arrived at probe 3B, and at t = 49.83 hours it arrived at 3C. The maximum cannot with any level of certainty be detected in probe

3D. The diurnal fluctuation can easily be seen 10.3 meters into the bar at probe 3B. Probe 3D, at 20.7 meters away from the river, yields no discernible diurnal fluctuation in temperature.

3.3.2 Model Data

3.3.2.1 GMS 6.0: MODFLOW/MODPATH

The three-dimensional ground water flow model was created to simulate hyporheic flow path geometry. Figure 3.4 (top left) presents the potentiometric surface map for the gravel bar and the surrounding area. The flow path geometry displayed in Figure 3.4 (top right) confirmed that the instrumentation array rows were oriented parallel to hyporheic flow through the bar. The root mean squared error for the observed head versus the calculated head was 0.02 m. Through inspection of the potentiometric map, two distinct areas could be distinguished. The first area, the peninsula, was characterized by a hydraulic gradient slope of 5%. The remaining area, the point bar base and base/island body, was characterized by an average hydraulic gradient of 2%. The geometric mean of hydraulic conductivity values used to calibrate the model was 7.87 E-03 m s^{-1}. The porosity used in the simulation was 0.36 m^3 m^{-3}.

3.3.2.2 HYDRUS

Using the hydraulic properties determined in GMS MODFLOW (hydraulic conductivity, porosity), a simplified two dimensional water and heat transport model was constructed using HYDRUS 3D. The model was built to estimate the thermal properties of the aquifer and simulate movement of the river water heat signature as it travelled through the hyporheic zone. The Marquardt-Levenberg type parameter optimization algorithm built into HYDRUS was used for the inverse estimation of the aquifer thermal properties using DTS temperature data from the river, surface, and fiber optic probe 2B. Initial estimates for the volumetric heat capacity of the solid and liquid phases were determined using commonly accepted literature values (2.0 E6 J m^{-3} °C^{-1} and 4.2 E6 J m^{-3} °C^{-1}, respectively). The apparent thermal conductivity parameters were set using visual best fit comparison between the temperature profile of DTS probe 2 B and the computed result (Figure 3.5). Average pore water velocity

was calculated as 7.7E-05 m s^{-1}, which is 58% smaller than the pore water velocity calculated from a saltwater tracer test (1.83 E-04 m s^{-1}). The volumetric heat capacity of the solid phase was calculated as 3.0 E6 J m^{-3} °C^{-1} and the volumetric heat capacity of the liquid phase was determined to be 4.2 E6 J m^{-3} °C^{-1}. The liquid phase fraction was equal to the porosity, 0.36, and the solid phase fraction was 0.64.

Figure 3.6 illustrates the result of the sensitivity analysis scenarios. The first scenario, in which the gravel bar surface temperature was held constant at the weekly average, the hyporheic temperature diverged from the calibrated result becoming cooler. In the second scenario, no discernable difference from the calibrated version was observed.

3.3.3 Energy Balance Calculations

Based on the theory presented in Peixoto and Oort [1992], we define our conceptual model for a control volume as illustrated in Figure 3.7. The heat content for the hyporheic zone is the sum of the heat fluxes across the boundaries of the control volume. This can be mathematically expressed as:

(3.1)

$$L\frac{\partial Q_{hz}}{\partial t} = qQ_{wi} - qQ_{wo} + LG_{wt} - LG_{aq}$$

Where Q is the heat content [J m^{-2}] of a layer of length L [m]. G represents the conductive heat fluxes [W m^{-2}] at the top and bottom boundaries of the layer, and q is specific discharge [m s^{-1}]. Subscripts *hz*, *wi*, *wo*, *wt*, and *aq* represent the hyporheic zone, advected water in, advected water out, water table and deep aquifer, respectively. Assuming uniform specific heat and density throughout the layer, heat content can be defined as:

(3.2)

$$Q = hc\rho T$$

Or

$$Q = hCT$$

Where c is specific heat [J kg^{-1} °C^{-1}], ρ is density [kg m^{-3}], C is the volumetric heat capacity [J m^{-3} °C^{-1}], and T is the depth-averaged temperature [°C] of a layer with thickness h [m]. The conductive fluxes are defined as:

(3.3)

$$G = k\frac{\partial T}{\partial z}$$

Where k is the thermal conductivity [W m^{-1} °C^{-1}] of the layer and $\partial T/\partial z$ [°C m^{-1}] is the vertical temperature gradient within the layer at the boundary. By substitution of equations 2 and 3 into equation 1, we obtain:

(3.4)

$$Lh_{hz}C_{hz}\frac{\partial T}{\partial t} = qh_{hz}C_w(T_{in} - T_{out}) + L\left(k\frac{\partial T}{\partial z}\right)\Big|_{wt} - L\left(k\frac{\partial T}{\partial z}\right)\Big|_{aq}$$

The subscript w is for the designation of water. The term on the left hand side of equation 4 represents the net energy change within the system. Positive values indicate a net gain in internal energy over time and negative values represent a net loss within the volume. The first term on the right side of the equation is the net energy flux from advective flow. The second term is the net heat flux across top boundary, and the third term is the net heat flux across the bottom boundary. The top boundary coincided with the elevation of the water table within the gravel bar. The bottom boundary was to ideally be located at the interface of the hyporheic zone and a deeper aquifer. However, owing to the difficulty in inserting the temperature probes into the coarse gravel of the bar, we were only able to collect temperature data to a depth of 1.3 m below the water table at limited locations. 1 m below the water table at fiber optic probes 2B and 2C, the mean vertical temperature gradient was 0.3 °C m^{-1} with a range of 0.9 °C m^{-1}. The mean vertical gradient at the top boundary was -1.1 °C m^{-1} with a range of 26.1 °C m^{-1}. Due to the limited data collected and the comparatively small vertical temperature gradient at the bottom boundary, it is assumed that the net flux across this boundary is near zero. Equation 4 then becomes:

(3.5)

$$Lh_{hz}C_{hz}\frac{\partial T}{\partial t} = qh_{hz}C_w(T_{in} - T_{out}) + L\left(k\frac{\partial T}{\partial z}\right)\Big|_{wt}$$

The thermistor data in Figure 3.3 qualitatively indicated an increase in average temperature in the hyporheic zone as water flowed across the gravel bar. Since the vertical flux across the bottom boundary can be neglected and the net advective flux and change in heat content with time can both be measured, the net flux across the water table boundary can be expressed as:

(3.6)

$$k\frac{\partial T_{wt}}{\partial z} = h_{hz}C_{hz}\frac{\partial T}{\partial t} - \frac{qh_{hz}C_w(T_{in} - T_{out})}{L}$$

Using the thermal parameters determined from the HYDRUS simulation (volumetric heat capacities of solid/liquid phases and the associated phase fractions) and the thermistor temperature data, the heat flux across the water table boundary of the hyporheic zone was calculated from the edge of the wetted perimeter of the river to 20.69 m across the bar (location of thermistor probe 3D). Positive values represent heat flowing into the layer and negative values represent heat flowing out of the layer. Note that the volumetric heat capacity of the hyporheic zone, C_{hz}, was calculated as the sum of the solid/liquid phase fractions multiplied by their respective volumetric heat capacities. The volumetric heat capacity of the hyporheic zone was found to be 3.4 E+06 J m^{-3} °C^{-1}. The value used for volumetric heat capacity of water was 4.2 E+06 J m^{-3} °C^{-1}. The total length across the hyporheic zone was partitioned into the zones: river–3A, 3A–3B, 3B–3C, and 3C–3D. The 24 hr average fluxes across the water table for each zone and the average flux for the total region are presented in Figure 3.8. The average flux across the water table for the entire observation period was 3.3 W m^{-2}.

3.4 Discussion

In this study, the hyporheic zone of a young gravel bar on a large gravel bed river was characterized and delineated in order to determine the contributing sources and sinks of heat within the zone. The initial finding of this study was that as stream

water flowed across the hyporheic zone of this particular gravel bar, the mean temperature of stream water increased. After developing a conceptual framework to quantify the fluxes of heat within the hyporheic zone, it was determined that the net gain in heat within the hyporheic zone was attributed to heat flux from the vadose zone, across the water table, into the hyporheic zone.

This study was motivated by the need to understand how the energy content of stream water could potentially be lowered by flowing through the hyporheic zone. Our study found that stream water energy content was not lowered, but rather, stream water energy was elevated via travel through the hyporheic zone. These findings were contrary to the findings reported from previous studies of hyporheic exchange on the Willamette River. [*Fernald et al.,* 2006] observed that the emergent water from the hyporheic zone tended to have a lower temperature than the water entering the hyporheic zone. They posited that the physical processes likely to cause cooling in the hyporheic zone were (1) conduction with substrate and (2) the mixing of surface temperature and hyporheic water (free convection). Though conduction was among the primary physical processes of heat exchange in this study, no evidence was found indicating conduction with deeper sediments would cause a net cooling effect of the stream water as it passed through the hyporheic zone. Also, no evidence was found to suggest that free convection or hyporheic water mixing with the lower aquifer was occurring. The fiber optic profiles revealed thermal stratification in the hyporheic zone.

Processes influencing heat flux to the stream

With regard to temperature dynamics in the hyporheic zone, this study found the source of the heat added to the system was due to heat flux from the vadose zone into the hyporheic zone. While studies analyzing hyporheic exchange longitudinally oriented to the stream channel can discount the vadose zone, this study could not. Previous research [*Fernald et al.,* 2001; *Fernald et al.,* 2006] on the Willamette River focused on hyporheic exchange laterally oriented to the stream channel, whereas this study focused on exchange across a gravel bar with an unsaturated zone. Since a heat

balance was not performed on the vadose zone, we cannot definitively state which source (solar radiation, convection (wind), latent heat, etc.) was most significantly affecting the heat content of the vadose zone. That notwithstanding, it is likely that the primary sources of heat in the vadose zone were a combination of solar radiation (insolation) and convective mixing.

The lack of shading of the gravel surface of the bar likely facilitated increased solar radiation absorption [*Johnson*, 2004]. Additionally, the sensitivity analysis of the temperature transport model, in which the gravel bar surface temperature was held constant at the weekly average, found that when the fluctuation in daily surface heating was removed, the hyporheic temperature was lowered. This evidence further supported the assumption that solar radiation was the primary source of heat affecting the vadose zone.

Indirect evidence suggesting that convective mixing was possibly occurring in the vadose zone was observed in the form of the depth of penetration of the diel surface fluctuation. A commonly accepted value for the maximum penetration of a diel temperature signal is a depth of 0.40 m [*Hillel*, 1998; *Peixoto and Oort*, 1992]. The temperature data collected by the fiber optic DTS probes reveal the diel temperature signal penetrating the vadose zone until contact with the water table, 0.50 m depth. These results suggest that a process aside from conduction may be responsible for the increased transport of heat from the surface downward. One such process would be barometric pumping. The daily variation in atmospheric pressure combined with the highly permeable vadose zone of the gravel bar could alter the gas pressure gradients causing heat to be transported more quickly [*Pirkle et al.*, 1992].

Given that the heat flux into the hyporheic zone had its source in the vadose zone, it was expected that the magnitude of the heat flux would possibly be associated with the height, or thickness, of the vadose zone above the water table. Figure 3.8 reveals that each zone, river–3A, 3A–3B, 3B–3C, and 3C–3D, contributed similar amounts of energy to the hyporheic zone. Zone 3C–3D, on average, contributed the largest flux of heat. The average depths to the water table for each zone were 0.19 m,

0.45 m, 0.60m, and 0.63 m (river–3A through 3C–3D, respectively). Combined with the findings from the previous chapter, this suggests that the depth to the water table is not the limiting factor. In the previous chapter, it was observed that the propagation rate of heat slowed dramatically in the area of the capillary fringe. This suggests that the capillary fringe can limit the heat flux rate into and out of the saturated zone. Furthermore, since the fringe is likely to be relatively constant in space, the main sensitivity must be the magnitude and duration of solar radiation.

At a broader scope, the results of this study provide a more comprehensive conceptual framework with which the energy dynamics of the hyporheic zone can be integrated into total stream energy. The objective of our study was to identify key thermal parameters and develop a comprehensive heat balance for a characteristic gravel bar. When this study began, it was assumed the vadose zone would have minimal influence on the temperature dynamics within the hyporheic zone. The depth of the vadose zone was expected to have sufficient thickness, e.g. > 0.40 m, to insulate the hyporheic zone from short term surface heating. However, the fiber optic probe profiles clearly reveal that ~0.50 m of gravel media is not sufficient to insulate the hyporheic zone from short term fluctuations. The short term heating of the hyporheic zone observed in this study is likely due to a lagged response of the heating of the vadose zone sediments. While it is beyond the scope of the data collected here to determine whether that is indeed the case, this would be an important area of future research on heat transport in stream environments.

This study is among the few which attempt to determine the role of the hyporheic zone in the thermal regime of a large gravel bed stream. Most studies of hyporheic heat exchange have been limited to smaller stream systems. Studies such as Johnson [2004] and Arrigoni et al. [2008] both evaluated smaller streams that have a higher ratio of hyporheic discharge to in-stream flow. While the processes governing heat transport within the hyporheic zone of such streams are the same as the processes in a larger stream, such as the Willamette, the magnitude of the influence of these

processes can differ. The dominant bed processes outlined in Evans et al. [1998], such as net bed radiation, are not as relevant in stream systems with significant depth.

Other studies conducted by Burkholder et al. [2008] and Fernald et al. [2006] which examined larger river systems, found that the outflow from gravel bars was cooler than mainstream temperatures. Burkholder additionally found that the temperatures of hyporheic outflows varied over the day and might be warmer than the mainstem at night. However, their conclusions were based on the temperature inputs and outputs with little confirmation of hyporheic flow path geometry. Therefore, it is not clear that the decreased temperatures observed were due to a cooling effect within the hyporheic zone or simply a lagged temperature signal. As a result, these studies provide little information regarding the hyporheic processes governing output temperature.

With respect to stream management and restoration; hyporheic connectivity has increasingly been considered as a method to mitigate thermal pollution in streams [*Arrigoni et al.*, 2008; *Burkholder et al.*, 2008; *Fernald et al.*, 2001; *Fernald et al.*, 2006; *Seedang et al.*, 2008]. One such method of increasing hyporheic connectivity would be to augment the stream sediment load via the addition of sediments characteristically similar to the bed and bank sediments [*Elkins et al.*, 2007]. However, based on the findings of this study, engineering gravel bars of similar geometry as the one analyzed here could potentially add heat to the overall stream system. The results of this research indicate the need to understand the potential for both warming and cooling of flow through the hyporheic zone, depending on the physical properties of the channel and gravel. This should be taken into account before investing in engineering projects intended to mitigate the effects of flows at temperatures above recommended levels.

Limitations of this study

The first limitation of this study is that the observations are limited to a single gravel bar. It is not clear whether hyporheic heat would behave similarly on gravel bars with surface shading via well established plant communities. Using the

descriptions provided in Fernald et al. [2006], “middle’ and “old” aged gravel bars on the Willamette may have smaller gains in heat due to the establishment of plant communities providing shading of the ground surface.

Secondly, while our measurements did not indicate a large interaction occurring between hyporheic water with a deeper aquifer, our observations were limited to the depth to which hyporheic temperatures were recorded and the definition of the bottom boundary of the heat transport conceptual model. While conventional thought would be to determine the depth at which the flow in the hyporheic zone is no longer hydraulically influenced by pressure gradients generated by the river, the MODFLOW results indicate that this depth does not exist in the 10 m vertical domain that had been simulated. As a result, the bottom boundary was chosen using deepest temperature measurements we were able to obtain. The deepest temperature measurements were made using the DTS system. As a result we were only able to obtain a value of the bottom flux between fiber optic probes 2B and 2C. Despite this limitation, the lack of a strong variable gradient at the base of the probe indicates that thermal exchange is minimal.

While river engineering to enhance hyporheic flow may still be a viable means to mitigate thermal pollution in streams such as the Willamette, the results of this study indicate that attributes such as the physical setting and vegetation cover of engineered gravel features may be critically important in determining their effectiveness in reducing stream temperatures. Geomorphic features which have similar characteristics to the gravel bar characterized in this study (e.g. age, geometry, plant community establishment), are likely to add heat to the stream system and negatively impact thermal heterogeneity. Therefore, future research regarding the impact of hyporheic flow on the thermal regime of streams should consider the relationship between the hyporheic zone and the vadose zone, the effects of plant community establishment on the hyporheic zone, and gravel bar geometry.

3.5 Conclusions

Our study examined the flow of water through the hyporheic zone of a young unvegetated gravel bar on the mid Willamette River (240 rkm) in late summer. The gravel bar was instrumented using an array of temperature sensors that captured the temperature signature of the stream water as it flowed through the hyporheic zone of the gravel bar. As discussed by Arrigoni et al. [2008], the daily maxima were attenuated and retarded as water flowed along the hyporheic pathway. However, no evidence of cooling was observed. We observed the amplitude of the thermal signal decrease along a hyporheic flow path, while the average hyporheic temperature increased. Our measurements confirmed that heat transport was predominantly driven by advective flow. However, using a simple layer control volume approach, a heat budget was calculated and determined surface heating was an additive source of heat, via vadose zone storage and transport. In comparison, a relatively negligible flux was observed at the lower layer boundary. The findings of this study suggest the impact of surface shading, gravel bar geometry and vadose zone processes should be considered in future investigations regarding temperature dynamics of hyporheic exchange in large gravel bed rivers.

3.6 Figures

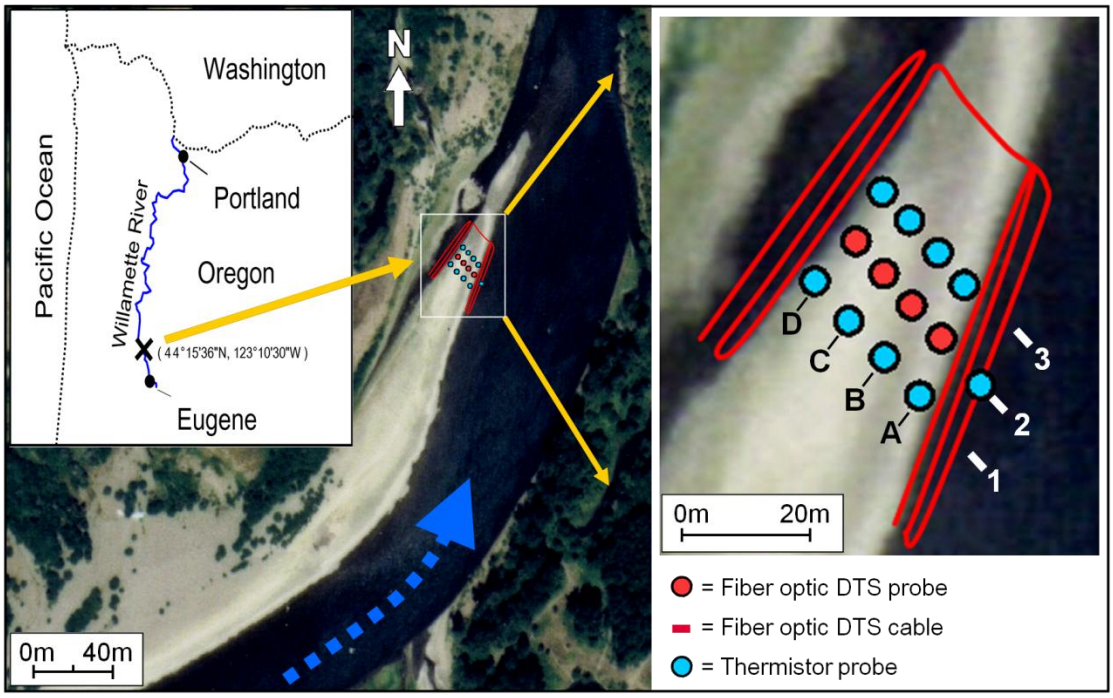

Figure 3.1 Site description and instrumentation layout

The site is located on the Willamette River at river km 261. The image at top right contains the layout of the temperature instrumentation. The armored cable is laid out in two serpentine configurations, beginning in the alcove then spanning across the surface of the gravel bar and ending in the river. The fiber optic probes are on row 2 (A–D). The thermistor probes are rows 1&3 (A–D).

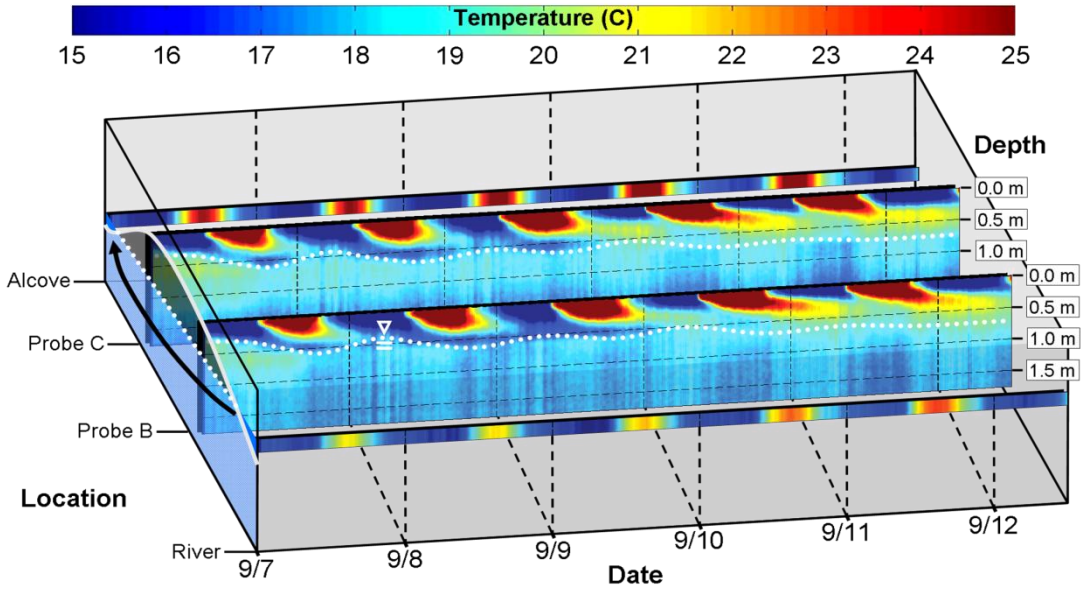

Figure 3.2 Fiber optic distributed temperature sensing (DTS) data summary

A summary of the fiber optic DTS data collected on the site. Each time series trace is arranged according to their orientation on the gravel bar (see Figure 1). The river and alcove temperature traces represent the averages from their respective configurations. The dotted lines on the probe traces represent the variation in the water table over the sampling period. The daily heat flux from the surface can readily be seen as well as the fluctuation of the temperature in the hyporheic zone.

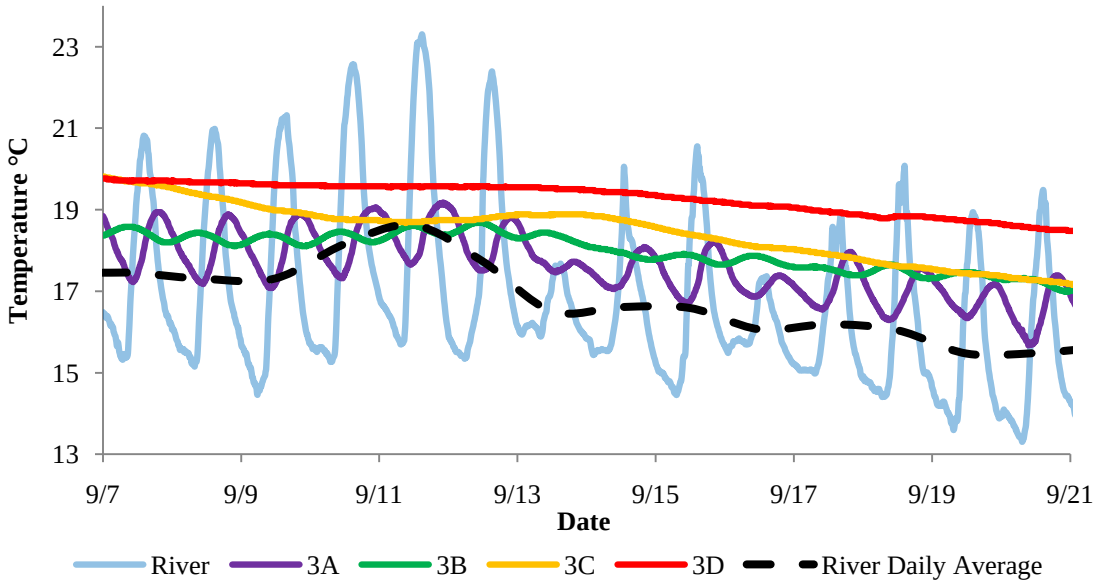

Figure 3.3 Thermistor Data

The thermistor probe data shown here are from row 3 probes A–D and a V2 thermistor located in the river (see figure 1 for layout). The 6th dataset is the average daily temperature of the river.

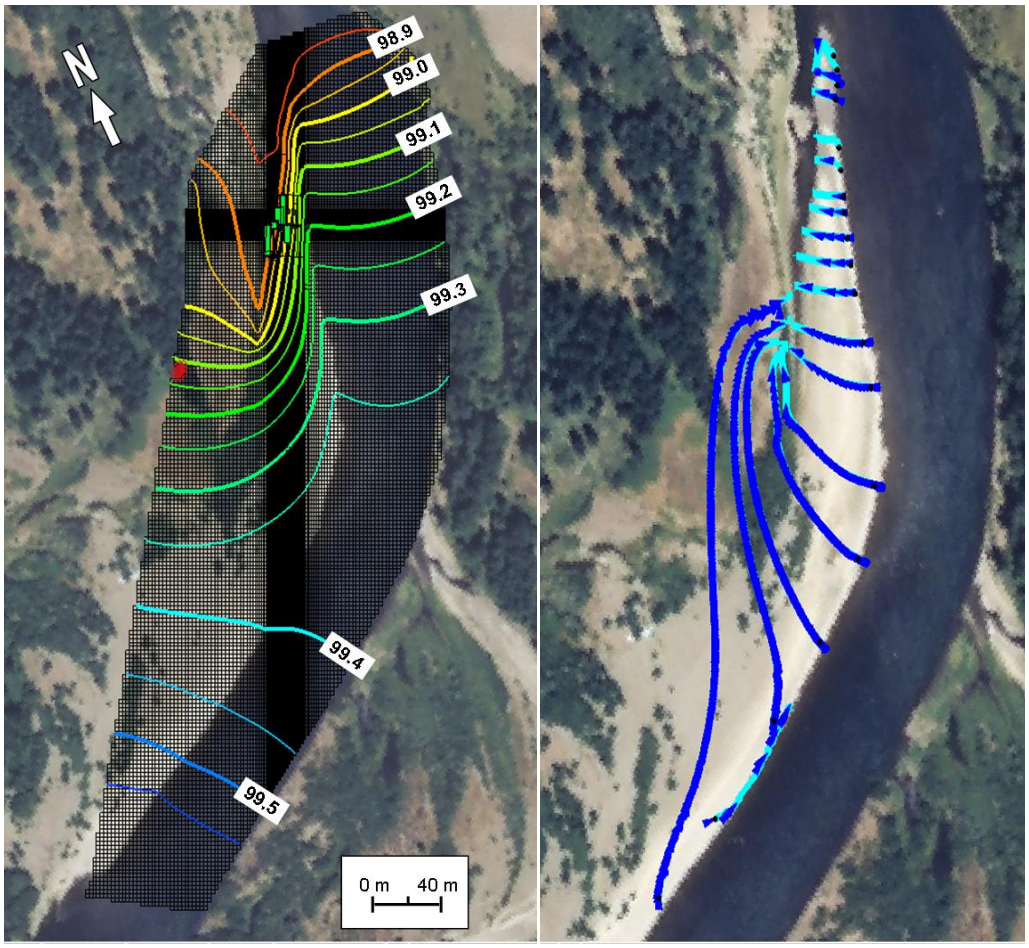

Figure 3.4 GMS result

The left is the potentiometric surface map and the right is the orientation of hyporheic flow paths through the instrumentation array.

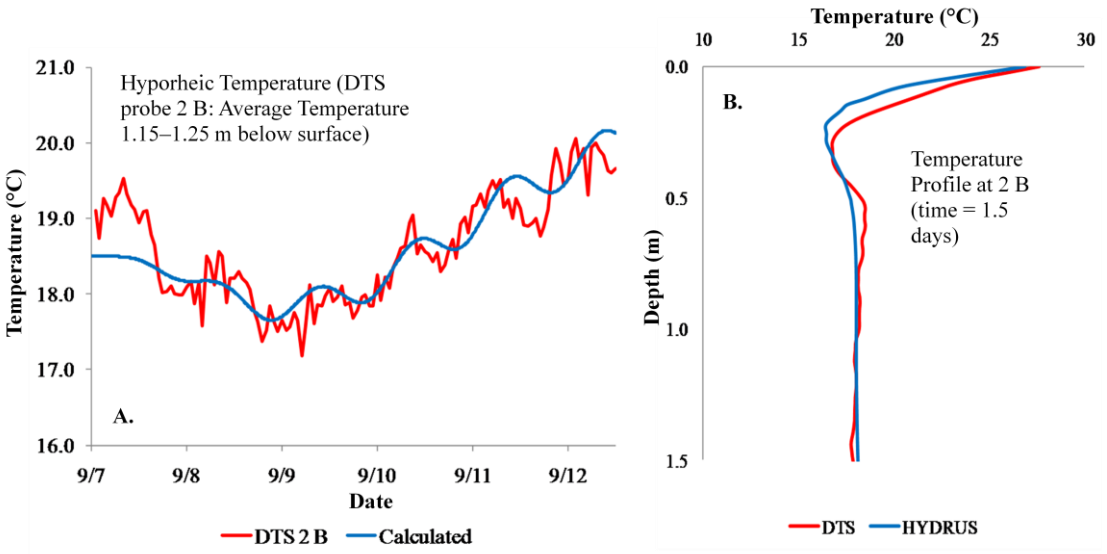

Figure 3.5 HYDRUS result

Plots demonstrate the "fit" of the observed data versus the calculated data from the model simulation. The plot on the left demonstrates the "fit" of the model to an observed area over time, and the plot on the left illustrates the "fit" of multiple points at one given time.

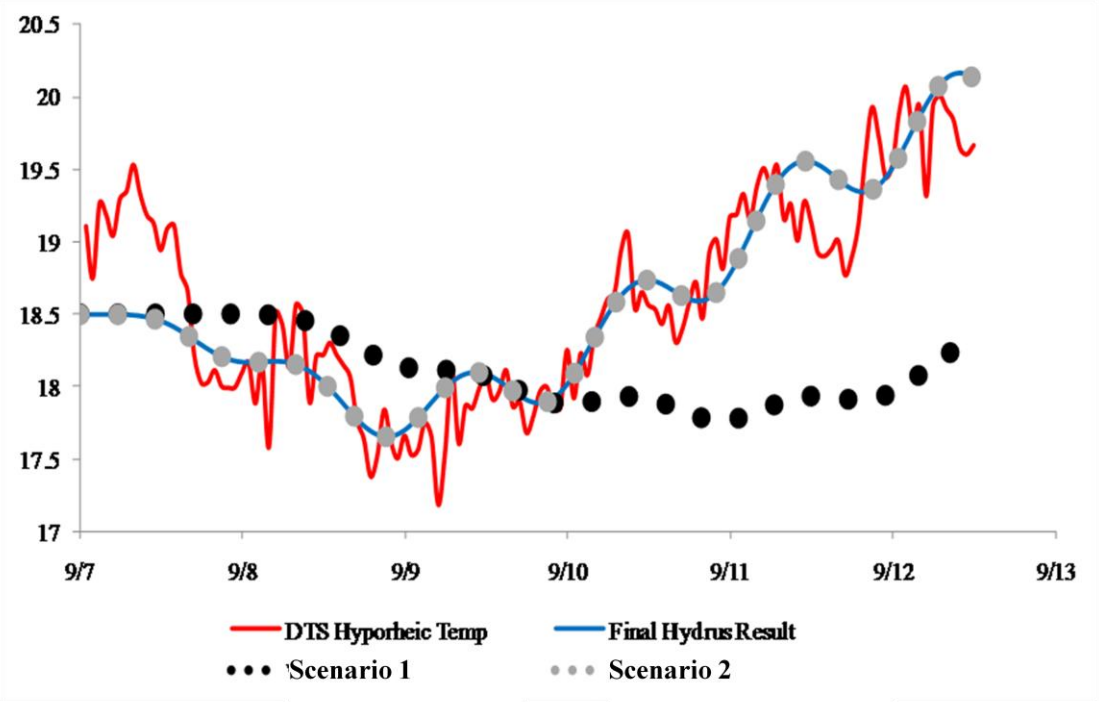

Figure 3.6 HYDRUS sensitivity analysis scenarios

Sensitivity analysis of the temperature transport model. Scenario 1: the gravel bar surface temperature was held constant at the weekly average. Scenario 2: a cooler region was created in the lower portion of the model domain to simulate hyporheic flow mixing with a cooler, deeper aquifer. Scenario 1 generated a marked difference, while scenario 2 yielded no discernible difference from the calibrated simulation.

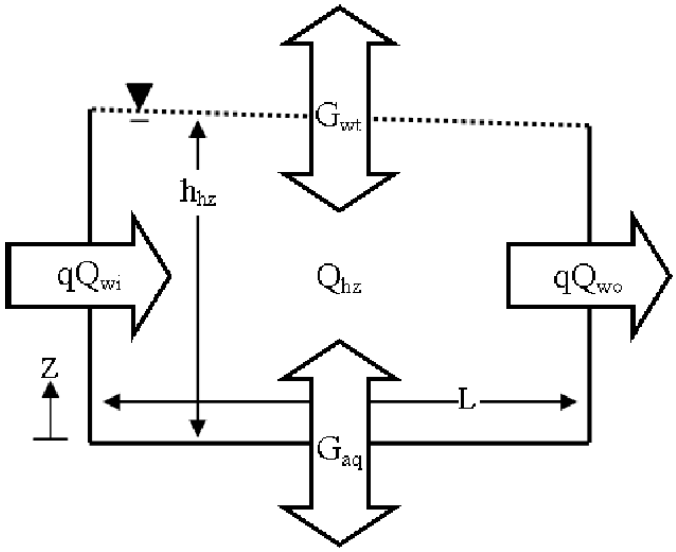

Figure 3.7 Conceptual diagram of the hyporheic zone

Diagram for the control volume representing the hyporheic zone. Parameters represented are: Heat content, Q [J m^{-2}]; conductive flux, G [W m^{-2}]; advective flux, qQ [W m^{-1}]; average pore water velocity, q [m s^{-1}] and the height and length, hhz and L [m], respectively.

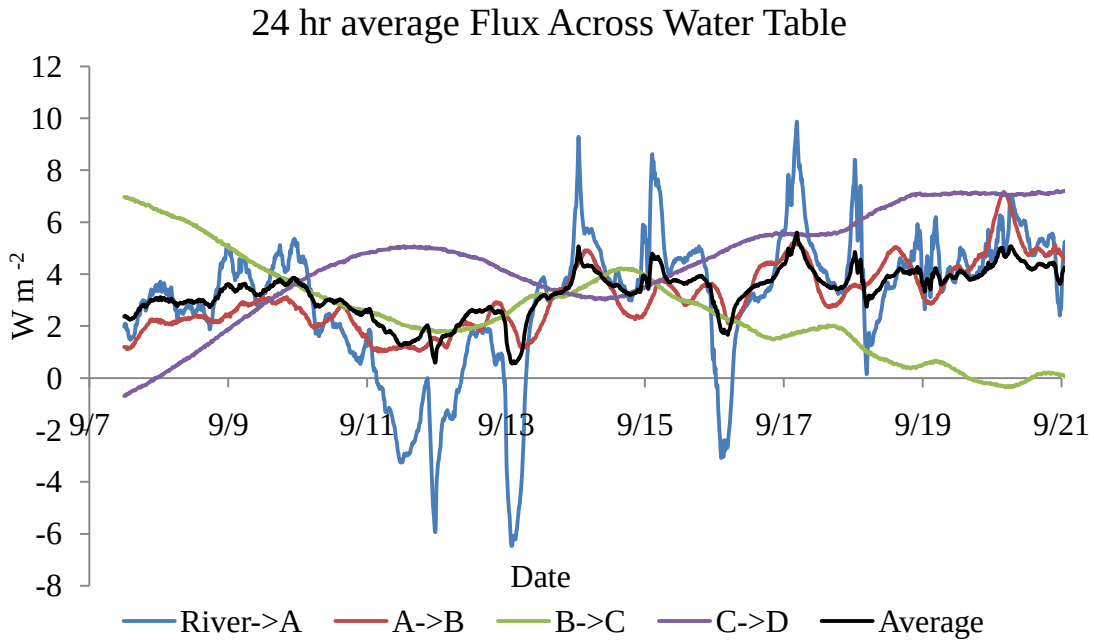

Figure 3.8 24 hr average heat fluxes across the water table

Each trace represents the 24 hr average heat (W m^{-2}) flux across the water table. The average flux of heat across the water table for the sample period was 3.3 W m^{-2}.

3.7 Tables

Table 3.1 HYDRUS thermal parameters

Parameter	Value
Solid Fraction Volumetric Heat Capacity [J m^{-3} K^{-1}]	3.0E+06
Solid Fraction [m^3 m^{-3}]	0.64
Liquid Fraction Volumetric Heat Capacity [J m^{-3} K^{-1}]	4.2E+06
Liquid Fraction [m^3 m^{-3}]	0.36
Longitudinal Dispersion [m]	0.41
Transverse Dispersion [m]	0.01
Saturated Apparent Thermal Conductivity [W m^{-1} C^{-1}]	2.5
q velocity [m day^{-1}]	6.72

Chapter 4: References

Agilent Technologies (2007), N4385A_DTS_Users_Guide.pdf, edited, p. 72, Böblingen, Germany.

Arrigoni, A. S., G. C. Poole, L. A. K. Mertes, S. J. O'Daniel, W. W. Woessner, and S. A. Thomas (2008), Buffered, lagged, or cooled? Disentangling hyporheic influences on temperature cycles in stream channels, *Water Resour Res*, *44*(9), -.

Bach, W., N. R. Banerjee, H. J. B. Dick, and E. T. Baker (2002), Discovery of ancient and active hydrothermal systems along the ultra-slow spreading Southwest Indian Ridge 10 degrees-16 degrees E, *Geochemistry Geophysics Geosystems*, *3*, 15.

Burkholder, B. K., G. E. Grant, R. Haggerty, T. Khangaonkar, and P. J. Wampler (2008), Influence of hyporheic flow and geomorphology on temperature of a large, gravel-bed river, Clackamas River, Oregon, USA, *Hydrol Process*, *22*(7), 941-953.

Constantz, J., and C. L. Thomas (1996), The use of streambed temperature profiles to estimate the depth, duration, and rate of percolation beneath arroyos, *Water Resour Res*, *32*(12), 3597-3602.

Elkins, E. M., G. B. Pasternack, and J. E. Merz (2007), Use of slope creation for rehabilitating incised, regulated, gravel bed rivers, *Water Resour Res*, *43*(5), -.

Evans, E. C., M. T. Greenwood, and G. E. Petts (1995), SHORT COMMUNICATION THERMAL PROFILES WITHIN RIVER BEDS, *Hydrol Process*, *9*(1), 19-25.

Evans, E. C., G. R. McGregor, and G. E. Petts (1998), River energy budgets with special reference to river bed processes, *Hydrol Process*, *12*(4), 575-595.

Fernald, A. G., and S. J. Guldan (2006), Surface water-groundwater interactions between irrigation ditches, alluvial aquifers, and streams, *Reviews in Fisheries Science*, *14*(1-2), 79-89.

Fernald, A. G., P. J. Wigington, and D. H. Landers (2001), Transient storage and hyporheic flow along the Willamette River, Oregon: Field measurements and model estimates, *Water Resour Res*, *37*(6), 1681-1694.

Fernald, A. G., D. H. Landers, and P. J. Wigington (2006), Water quality changes in hyporheic flow paths between a large gravel bed river and off-channel alcoves in Oregon, USA, *River Res Appl*, *22*(10), 1111-1124.

Geist, D., T. Hanrahan, E. Arntzen, G. McMichael, C. Murray, and Y. Chien (2002), Physicochemical Characteristics of the Hyporheic Zone Affect Redd Site Selection by

Chum Salmon and Fall Chinook Salmon in the Columbia River, *N Am J Fish Manage*, *22*, 1077-1085.

Hannah, D. M., I. A. Malcolm, C. Soulsby, and A. F. Youngson (2004), Heat exchanges and temperatures within a salmon spawning stream in the cairngorms, Scotland: Seasonal and sub-seasonal dynamics, *River Res Appl*, *20*(6), 635-652.

Harding, J. S., E. F. Benfield, P. V. Bolstad, G. S. Helfman, and E. B. D. Jones (1998), Stream biodiversity: The ghost of land use past, *Proceedings of the National Academy of Sciences of the United States of America*, *95*(25), 14843-14847.

Harris, R. N., and D. S. Chapman (1997), Borehole temperatures and a baseline for 20th-century global warming estimates, *Science*, *275*(5306), 1618-1621.

Harris, R. N., and D. S. Chapman (2007), Stop-go temperature logging for precision applications, *Geophysics*, *72*(4), E119-E123.

Harrisburg USGS Gauge 14166000 (2007).

Hillel, D. (1998), *Environmental Soil Physics*, 771 pp., Academic Press, London, UK.

Hurtig, E., S. Grosswig, M. Jobmann, K. Kuhn, and P. Marschall (1994), FIBEROPTIC TEMPERATURE-MEASUREMENTS IN SHALLOW BOREHOLES - EXPERIMENTAL APPLICATION FOR FLUID LOGGING, *Geothermics*, *23*(4), 355-364.

Johnson, S. L. (2004), Factors influencing stream temperatures in small streams: substrate effects and a shading experiment, *Can J Fish Aquat Sci*, *61*(6), 913-923.

Keery, J., A. Binley, N. Crook, and J. W. N. Smith (2007), Temporal and spatial variability of groundwater-surface water fluxes: Development and application of an analytical method using temperature time series, *J Hydrol*, *336*(1-2), 1-16.

Laenen, A., and D. Dunnette (Eds.) (1997), *River Quality Dynamics and Restoration*, CRC Press, Boca Raton.

Loheide, S. P., and S. M. Gorelick (2006), Quantifying stream-aquifer interactions through the analysis of remotely sensed thermographic profiles and in situ temperature histories, *Environmental Science & Technology*, *40*(10), 3336-3341.

McDonald, M., and A. Harbaugh (1988), A Modular Three-Dimensional Finite Difference Groundwater Flow Model, edited, US Geological Survey, Reston, Virginia.

National Marine Fisheries Service (1999), Endangered Species Act Proposed 4(d) Rule for Pacific Salmon, edited by NMFS, Northwest Region.

O'Conner, J., A. Sarna-Wojcicki, K. Wozniak, D. Polette, and R. Fleck (2001), Origin, Extent, and Thickness of Quarternary Geologic Units in the Willamette Valley, Oregon, edited.

Oregon Climate Service (2007), The Climate of Oregon, edited by O. C. Service.

Peixoto, J., and A. Oort (1992), *Physics of Climate*, American Institute of Physics, New York.

Pirkle, R. J., D. E. Wyatt, V. Price, and B. B. Looney (1992), Barometric Pumping: The connection between the vadose zone and the atmosphere., paper presented at The Focus Eastern Regional Ground Water Issues Conference., Ground Water Managment, Newton, MA.

Pollack, H. N., and J. E. Smerdon (2004), Borehole climate reconstructions: Spatial structure and hemispheric averages, *Journal of Geophysical Research-Atmospheres*, *109*(D11), 9.

Poole, G. C., and C. H. Berman (2001), An Ecological Perspective on In-Stream Temperature: Natural Heat Dynamics and Mechanisms of Human-Caused Thermal Degradation, edited, pp. 787-802, Springer-Verlag New York Inc.

Quinn, B., F. Gagne, and C. Blaise (2004), Oxidative metabolism activity in Hydra attenuata exposed to carbamazepine, *Fresen Environ Bull*, *13*(8), 783-788.

Quinn, T. P., S. Hodgson, and C. Peven (1997), Temperature, flow, and the migration of adult sockeye salmon (Oncorhynchus nerka) in the Columbia River, *Can J Fish Aquat Sci*, *54*(6), 1349-1360.

Seedang, S., A. G. Fernald, R. M. Adams, and D. H. Landers (2008), Economic analysis of water temperature reduction practices in a large river floodplain: An exploratory study of the Willamette River, Oregon, *River Res Appl*, *24*(7), 941-959.

Selker, J. S., L. Thevenaz, H. Huwald, A. Mallet, W. Luxemburg, N. V. de Giesen, M. Stejskal, J. Zeman, M. Westhoff, and M. B. Parlange (2006), Distributed fiber-optic temperature sensing for hydrologic systems, *Water Resour Res*, *42*(12), 8.

Silliman, S. E., and D. F. Booth (1993), Analysis of Time-Series Measurements of Sediment Temperature for Identification of Gaining Vs Losing Portions of Juday-Creek, Indiana, *J Hydrol*, *146*(1-4), 131-148.

Silliman, S. E., J. Ramirez, and R. L. Mccabe (1995), Quantifying Downflow through Creek Sediments Using Temperature Time-Series - One-Dimensional Solution Incorporating Measured Surface-Temperature, *J Hydrol*, *167*(1-4), 99-119.

Šimůnek, J., M. van Genuchten, and M. Šejna (2005), The Hydrus-1D software package for simulating the one-dimensional movement of water, heat, and multiple solutes in variably-saturated media. Version 3.0, in *HYDRUS Software Series*, edited, Department of Environmental Sciences, University of California Riverside,, Riverside, CA.

Stallman, R. W. (1965), Steady 1-Dimensional Fluid Flow in a Semi-Infinite Porous Medium with Sinusoidal Surface Temperature, *Journal of Geophysical Research, 70*(12), 2821-&.

Story, A., R. D. Moore, and J. S. Macdonald (2003), Stream temperatures in two shaded reaches below cutblocks and logging roads: downstream cooling linked to subsurface hydrology, *Canadian Journal of Forest Research-Revue Canadienne De Recherche Forestiere*, *33*(8), 1383-1396.

Tufillaro, N., J. Dorighi, M. Collier, and J. Selker (2007), Measuring stream dynamics with fiber optics, *Agilent Measurement Journal*, *68*(3).

Tyler, S. W., J. S. Selker, M. B. Hausner, C. E. Hatch, T. Torgersen, C. E. Thodal, and S. G. Schladow (2009), Environmental temperature sensing using Raman spectra DTS fiber-optic methods, *Water Resour Res*, *45*, -.

Wallick, J. R., S. T. Lancaster, and J. P. Bolte (2006), Determination of bank erodibility for natural and anthropogenic bank materials using a model of lateral migration and observed erosion along the Willamette River, Oregon, USA, *River Res Appl*, *22*(6), 631-649.

Wisian, K. W., D. D. Blackwell, S. Bellani, J. A. Henfling, R. A. Normann, P. C. Lysne, A. Forster, and J. Schrotter (1998), Field comparison of conventional and new technology temperature logging systems, *Geothermics*, *27*(2), 131-141.

Chapter 5: Appendices

Appendix A: Topographic Survey

A.1. Topographic Survey

The topographic mapping of the gravel bar and its surrounding area was performed through the combination of total station[8] and precision GPS[9] data. The survey was accomplished by walking an approximate 2 m (3 paces) grid-pattern over the surface of the gravel bar. The bed of the alcove was surveyed at approximately 2 m spacing (4 paces), and the area surrounding the gravel bar was measured at an approximate interval of 5 m (8 paces). The elevation was arbitrarily set relative to 100 m.

[8] Leica TCM-1100- electronic transit and electronic distance meter (EDM) with data storage capability. Stated accuracy: ±0.01 m vertically and horizontally at 100 m distance.

[9] Trimble Pathfinder- Using maximum resolution settings with radio telemetry correction, the accuracy stated as ±0.05 m

Table A.1. Topographic Survey Data

Easting	Northing	Elevation	Easting	Northing	Elevation
-4.952	234.605	98.363	-33.152	122.416	98.969
-16.791	181.641	98.263	-26.888	121.687	98.756
-23.804	180.958	98.943	-24.122	121.385	98.766
-8.560	180.820	98.609	-20.428	121.054	98.836
-5.948	180.120	98.832	-7.604	121.031	99.020
-23.790	178.370	98.954	-2.867	120.973	99.283
-20.040	178.179	98.489	-15.468	120.228	98.665
-13.541	177.290	98.471	-12.091	119.441	98.382
-6.847	176.736	98.763	-7.283	118.976	98.975
-23.524	174.697	98.940	-0.128	117.704	99.318
-16.387	173.988	98.337	-4.444	116.858	99.321
-5.352	173.025	99.053	-7.991	116.546	99.018
-8.894	172.768	98.621	-3.584	111.262	99.406
-6.717	172.226	98.873	1.134	111.229	99.314
-22.715	169.718	98.935	3.042	110.962	99.315
-7.222	169.285	99.016	-78.972	110.132	98.974
-19.579	169.264	98.455	-1.249	106.586	99.412
-4.319	169.074	99.106	-5.940	106.147	99.422
-11.969	167.790	98.450	-8.533	105.875	99.025
0.038	167.714	98.780	10.113	102.573	98.925
-8.355	166.889	98.910	-8.997	101.281	99.025
-4.502	164.901	99.136	-4.505	100.317	99.511
-3.000	163.946	99.144	-51.867	100.079	99.670
-9.056	162.950	98.977	0.412	99.512	99.468
-5.300	162.266	99.160	-32.973	99.443	98.970
-9.778	159.259	99.026	4.514	99.023	99.365
-30.465	158.998	99.423	-27.913	98.881	98.831
-7.345	157.910	99.195	-22.310	98.180	98.687
-41.285	157.790	99.457	-16.808	97.786	98.549
-26.916	154.302	98.929	-12.344	97.666	98.400
-9.308	154.007	99.189	-9.674	97.617	98.966
-13.574	153.613	98.311	-9.280	94.450	99.202
-22.341	153.595	98.381	5.108	94.380	99.376
-10.917	153.466	98.829	-10.083	94.282	99.020
-17.423	153.400	98.304	0.077	93.867	99.504
-10.775	150.122	98.999	-4.942	93.817	99.634
-9.030	149.633	99.199	-10.605	89.554	98.988
-10.393	146.040	99.023	-6.334	88.561	99.671
-9.647	145.901	99.118	-32.872	87.962	98.963
-24.668	143.835	98.469	-1.293	87.481	99.654
-19.463	143.731	98.347	-27.634	87.409	98.870

Table A.1. Continued

Easting	Northing	Elevation	Easting	Northing	Elevation
-28.976	143.651	98.938	3.185	86.708	99.511
-15.459	142.878	98.271	-21.653	86.544	98.688
-10.430	142.844	98.914	6.400	86.348	99.384
-49.956	140.001	99.271	-16.808	85.545	98.556
-6.865	132.029	99.070	-13.757	84.539	98.496
-7.465	129.082	99.025	-55.139	83.981	100.309
-6.314	128.579	99.173	-11.690	83.789	98.976
-4.378	125.340	99.273	-19.283	50.431	99.037
-7.162	124.853	99.025	-14.525	49.309	99.497
-58.643	123.593	99.614	-9.934	47.505	99.783
-12.327	82.144	98.993	-29.288	47.467	98.785
6.822	82.001	99.387	5.538	47.427	99.735
2.119	81.321	99.562	0.568	47.423	99.803
-7.130	81.095	99.722	-32.814	47.309	98.981
-2.566	80.920	99.706	-19.567	47.280	98.971
-50.540	79.693	100.158	-25.052	47.220	98.752
-13.507	78.042	98.982	-3.906	47.083	99.839
-11.362	77.215	99.521	10.273	47.025	99.515
-6.776	76.350	99.767	11.794	46.862	99.467
-32.285	75.462	98.978	-18.436	42.958	99.007
-1.878	75.035	99.719	12.315	42.243	99.468
7.656	74.965	99.423	7.320	42.053	99.694
-27.430	74.860	98.888	-2.314	41.840	99.804
2.937	74.758	99.623	-12.358	41.799	99.747
-21.392	74.296	98.763	2.807	41.757	99.802
-16.746	74.080	98.607	-15.416	41.646	99.467
-14.276	74.035	98.994	-7.370	41.622	99.846
9.186	70.042	99.436	-44.593	38.678	100.575
4.315	69.915	99.608	-18.968	38.497	99.013
-14.874	69.855	99.026	-41.219	38.265	100.258
-12.836	69.704	99.497	-82.066	38.046	98.958
-0.443	69.627	99.697	-32.360	37.818	98.977
-10.153	69.431	99.750	-28.992	37.499	98.808
-5.380	69.132	99.800	-14.918	37.374	99.406
-16.169	65.145	99.027	-25.243	37.253	98.749
-13.689	64.209	99.448	-10.140	36.127	99.722
-8.733	62.756	99.770	-77.021	35.582	100.179
-4.002	62.009	99.812	-4.871	34.719	99.858
0.833	61.386	99.775	0.554	33.570	99.786
-33.823	60.880	98.988	0.541	33.557	99.792
10.492	60.700	99.426	6.028	33.149	99.769

Table A.1. Continued

Easting	Northing	Elevation	Easting	Northing	Elevation
-8.245	8.807	99.820	24.996	-21.289	99.499
17.465	8.139	99.467	16.437	-21.839	99.666
10.526	7.973	99.690	-23.801	-22.113	99.145
15.583	7.948	99.510	-21.040	-24.728	99.488
5.187	7.637	99.898	-26.024	-24.873	99.036
0.135	7.613	99.954	-10.998	-25.283	99.889
-3.968	7.544	99.908	28.351	-25.815	99.523
-77.542	7.078	100.489	1.985	-26.068	100.056
-29.006	6.981	98.983	15.264	-26.234	99.731
-26.743	6.566	98.835	-28.144	-26.894	99.145
19.283	3.750	99.482	-23.984	-30.461	99.173
14.487	3.686	99.559	-21.239	-32.796	99.553
9.825	2.530	99.784	-28.251	-32.958	99.148
-24.270	1.985	98.980	-4.844	-35.531	100.119
-18.723	1.672	99.435	-23.749	-36.348	99.221
-13.881	1.619	99.707	-49.879	-36.618	100.603
-8.824	1.468	99.863	8.741	-37.528	99.953
5.032	1.325	99.919	16.219	-37.923	99.768
0.503	1.221	99.916	29.409	-38.612	99.520
-4.222	1.211	99.872	-28.080	-39.733	99.174
-28.154	-0.621	98.973	-22.714	-43.788	99.563
18.046	-44.457	99.830	8.291	-100.179	99.774
13.837	-44.569	99.701	12.584	-100.903	99.881
4.907	-44.578	100.033	24.986	-101.118	99.555
-10.969	-44.714	100.048	18.934	-101.813	99.866
31.319	-44.897	99.529	33.543	-103.714	99.550
-28.170	-46.517	99.185	-25.408	-110.592	100.234
44.196	-50.962	99.070	-21.754	-110.929	100.531
-10.885	-51.217	100.174	-19.899	-111.753	100.463
-5.388	-51.422	100.061	-7.306	-111.850	100.229
-27.923	-52.355	99.235	-20.539	-112.453	100.496
2.550	-52.508	100.048	5.538	-112.840	99.864
13.397	-53.796	99.750	13.009	-113.474	99.757
17.927	-54.351	99.821	-8.453	-113.805	100.187
-23.467	-55.529	99.493	17.405	-113.857	99.812
27.836	-56.132	99.519	-2.356	-113.952	100.003
-27.208	-57.727	99.286	-22.909	-114.381	100.499
-23.556	-60.602	99.454	5.712	-114.473	99.779
-10.609	-62.502	100.293	13.830	-114.623	99.806
-28.220	-62.652	99.409	31.405	-115.827	99.544
-3.540	-63.097	100.022	21.175	-115.883	99.718

Table A.1. Continued

Easting	Northing	Elevation	Easting	Northing	Elevation
5.524	60.691	99.621	15.714	32.944	99.451
-29.724	60.357	98.821	11.461	32.940	99.589
-74.987	60.254	98.968	-20.674	28.993	99.002
-23.430	59.153	98.719	-43.086	28.901	100.472
-18.241	58.089	98.978	-14.976	28.362	99.473
18.640	57.343	98.904	-25.702	28.042	98.783
-44.699	56.477	100.268	-31.514	27.895	99.005
10.814	55.547	99.450	16.174	27.839	99.460
-18.866	55.452	99.027	-9.997	27.662	99.776
5.769	55.061	99.641	10.664	27.353	99.586
-14.475	54.933	99.433	-4.817	27.171	99.867
1.014	54.884	99.783	5.608	27.150	99.736
-4.022	54.755	99.785	0.285	26.918	99.860
-8.993	54.289	99.784	-35.878	24.689	99.954
-21.303	24.502	99.006	5.388	-1.522	99.918
-16.250	23.068	99.428	20.038	-1.604	99.481
-77.912	22.881	100.364	-9.472	-1.646	99.884
-30.647	21.907	98.999	-1.774	-1.771	100.007
-11.125	21.795	99.733	13.337	-1.798	99.650
-27.283	21.522	98.736	-28.000	-6.674	98.976
-22.735	20.932	98.963	-25.441	-7.813	99.003
-5.769	20.688	99.854	-19.768	-8.305	99.440
-0.441	18.437	99.905	14.494	-8.550	99.761
4.362	18.284	99.802	22.938	-8.678	99.484
16.207	18.151	99.461	-11.221	-8.736	99.836
14.412	18.007	99.521	-2.720	-8.906	100.007
9.384	17.806	99.696	5.575	-9.001	99.927
-22.210	16.158	99.013	-28.597	-13.316	99.081
-17.963	15.184	99.325	22.017	-15.066	99.497
18.294	14.408	99.463	41.269	-15.371	99.002
12.922	14.092	99.547	16.757	-15.471	99.838
-7.727	13.896	99.807	-9.667	-15.556	99.897
7.775	13.729	99.730	-18.593	-15.625	99.597
-2.772	13.384	99.890	-24.276	-15.837	99.107
2.467	13.283	99.909	7.606	-16.048	99.885
-30.035	13.252	98.975	-1.019	-16.653	100.041
29.826	13.123	99.037	-28.698	-18.924	99.168
-26.388	13.001	98.856	-18.994	-18.931	99.546
-23.280	11.258	98.999	-10.168	-19.834	99.872
-18.459	10.292	99.345	-1.600	-20.619	100.011
-13.280	9.536	99.711	7.675	-20.803	99.881

Table A.1. Continued

Easting	Northing	Elevation	Easting	Northing	Elevation
0.443	-63.257	100.068	29.207	-117.013	99.534
8.073	-64.153	99.927	-24.272	-118.182	100.558
28.485	-64.524	99.541	-23.089	-120.404	100.539
-24.114	-64.858	99.342	-25.707	-121.230	100.604
-29.132	-68.442	99.551	40.946	-121.621	99.033
-19.520	-69.722	99.893	-26.654	-121.705	100.630
-12.674	-70.850	100.242	-7.243	-124.147	100.043
0.835	-73.322	100.038	-27.448	-125.670	100.646
7.188	-74.413	99.681	-25.465	-126.249	100.610
11.023	-75.307	99.914	-28.475	-126.817	100.657
-27.863	-75.541	99.662	-27.458	-128.640	100.668
27.035	-77.752	99.534	-9.535	-129.063	100.135
-25.079	-78.500	100.019	-8.153	-129.414	100.093
-27.848	-80.863	99.695	-1.027	-130.719	100.007
49.750	-80.889	99.066	3.537	-131.541	100.441
-19.033	-81.598	100.241	7.931	-131.975	99.984
-1.057	-83.388	99.941	14.380	-132.041	99.987
3.361	-84.750	99.615	10.776	-132.117	100.401
7.880	-86.021	99.873	18.273	-132.284	99.670
-28.639	-86.491	99.796	22.411	-132.660	99.508
26.216	-88.473	99.539	-8.941	-132.879	100.094
-22.206	-89.062	100.265	-26.783	-133.486	100.626
-5.309	-93.329	100.037	-1.605	-133.687	100.036
3.410	-95.682	99.887	3.737	-134.554	100.368
8.795	-96.879	99.793	-29.210	-134.739	100.692
11.349	-97.804	99.878	8.185	-135.023	100.224
-28.683	-98.592	99.992	11.862	-135.540	100.210
-4.836	-98.700	100.163	-30.356	-135.988	100.736
-28.870	-137.916	100.696	1.012	-176.168	99.459
17.327	-138.889	99.587	-55.482	-177.704	100.738
-9.314	-139.237	100.032	-110.492	-179.816	100.997
-4.832	-140.100	99.842	-68.295	-179.934	101.050
-28.222	-140.143	100.655	-44.116	-181.557	100.701
20.202	-140.146	99.512	-99.894	-184.558	101.237
-30.361	-140.301	100.675	-31.922	-186.455	100.256
0.058	-141.283	100.143	-88.672	-189.544	101.248
-31.402	-141.506	100.663	-19.526	-190.513	99.890
2.478	-141.692	100.017	-76.965	-192.691	101.273
10.251	-142.563	99.997	-8.531	-194.060	99.464
4.699	-142.612	100.435	-65.154	-196.359	101.124
-29.638	-142.800	100.667	-52.587	-200.001	100.724

Table A.1. Continued

Easting	Northing	Elevation	Easting	Northing	Elevation
-101.313	-294.444	100.538	106.413	157.999	99.972
-84.650	-297.628	99.843	113.361	127.904	100.327
-75.694	-299.511	99.538	118.160	87.682	99.915
-31.795	-143.019	100.690	-136.846	-203.381	100.660
5.811	-143.323	100.272	-40.759	-204.209	100.286
14.384	-143.324	99.748	-148.021	-205.487	100.707
-30.777	-143.604	100.698	-125.668	-206.689	101.119
6.728	-143.664	100.260	-29.575	-207.799	99.921
17.938	-144.806	99.520	-25.370	-210.289	99.795
-10.588	-148.954	99.959	-25.335	-210.295	99.686
-6.892	-149.755	99.817	-114.637	-210.359	101.499
-2.681	-150.388	100.043	-19.172	-211.650	99.464
1.544	-150.693	99.521	-102.931	-213.115	101.528
3.239	-151.542	99.351	-90.070	-214.056	101.393
7.336	-152.525	99.501	-122.741	-215.473	101.096
15.491	-154.463	99.533	-78.414	-215.804	101.118
19.078	-155.275	99.534	-65.957	-218.380	100.907
27.567	-163.072	99.019	-8.163	-219.274	98.844
-83.562	-11.384	100.959	-53.814	-221.670	100.521
-78.561	8.084	100.534	-41.912	-224.642	100.029
-75.289	35.401	100.333	-116.491	-227.477	101.360
-64.457	44.014	100.543	-139.639	-228.829	100.410
-25.232	-210.313	99.763	-30.387	-228.878	99.478
-47.608	-142.727	100.827	-128.242	-228.949	100.886
-36.502	-143.954	100.630	-100.426	-231.043	101.409
-29.007	-145.217	100.489	-84.524	-236.378	101.028
-20.688	-148.260	99.988	-69.544	-239.741	100.653
-9.251	-150.948	99.657	-53.637	-246.488	100.022
2.293	-153.773	99.747	-42.603	-251.374	99.494
-48.765	-154.851	100.967	-121.279	-262.191	101.215
-154.882	-155.676	99.166	-129.488	-262.710	101.278
14.158	-156.815	99.455	-105.463	-264.461	100.998
-39.349	-159.993	100.548	-89.560	-264.594	100.754
-88.107	-165.718	100.851	-73.285	-267.870	100.245
-28.331	-166.167	100.319	-56.334	-270.811	99.518
-16.684	-170.665	100.099	-50.928	-285.317	98.920
-79.537	-172.085	101.094	-133.363	-285.709	101.181
-5.613	-174.421	99.675	-117.015	-290.206	100.879
-135.483	-300.458	101.015	124.377	35.187	100.017
-119.911	-307.995	100.725	123.092	-32.075	100.317
-104.183	-311.478	100.103	122.647	-42.579	101.207

Table A.1. Continued

Easting	Northing	Elevation
-89.231	-318.723	99.577
-140.787	-319.799	100.597
-125.315	-324.994	100.420
-109.217	-329.520	99.911
-100.431	-332.249	99.598
-145.729	-335.055	100.920
-135.774	-337.972	100.336
-122.959	-340.695	100.037
-111.423	-344.290	99.637
-153.885	-351.519	100.637
-99.055	-353.017	99.100
-142.196	-354.629	100.178
-131.060	-359.233	99.901
-125.271	-362.437	99.648
-161.030	-369.678	100.468
-171.158	-369.865	100.672
-149.053	-374.803	100.011
-137.458	-378.052	99.687
-175.261	-385.255	100.464
-163.982	-388.939	100.149
-152.475	-392.553	99.845
-148.452	-394.474	99.690
-189.635	-401.170	100.449
-185.312	-403.812	100.395
-173.397	-408.057	100.047
-160.149	-410.325	99.715
-197.880	-417.732	100.513
-186.149	-420.912	100.136
-146.164	-422.030	99.261
-206.267	-422.987	100.797
-174.968	-425.357	99.827
-200.281	-426.344	100.327
-192.910	-429.048	100.117
-212.603	-439.620	100.252
-209.255	-440.804	100.262
-205.095	-442.985	100.134
-217.714	-446.594	100.436
-214.096	-446.658	100.270
-221.474	-446.757	100.878
-189.621	-450.077	99.645
-211.619	-452.216	100.224
118.600	-87.225	101.134
108.430	-132.439	99.884
100.992	-152.270	99.333
-26.400	-349.500	99.474
-51.300	-388.600	99.496
-70.760	-422.619	99.529
95.455	-163.732	99.308
88.061	-187.913	99.696
58.801	-232.229	99.599
47.767	-249.855	99.304
29.078	-282.077	100.826
17.582	-303.767	101.119
121.600	1.800	99.334
119.300	64.800	99.284
-68.317	104.671	99.996
-75.253	6.298	99.452
-86.338	-24.892	102.046
-94.156	-68.443	101.250
-100.471	-109.886	101.174
-36.604	-196.799	99.391
-47.480	-3.840	100.500
-45.150	12.520	100.450
-48.650	-20.190	100.550
-217.895	-469.750	99.804

Appendix B: Bathymetric Survey

B.1. Bathymetric Survey

The bathymetric survey was performed on the river channel approximately 400m upstream and 200m downstream of the gravel bar. The survey was accomplished by utilizing a nautical GPS system[10] that had the capability to record depth and horizontal position. combine those survey points with marked topographic survey points and water surface elevations of the river's edges. For this survey, the GPS antenna was oriented directly over the depth transducer. Points were recorded in UTM coordinates then translated to coordinate system of the topographic survey.

[10] Garmin GPSMAP® 185 Sounder- Manufacturer stated position accuracy is 1–5 m; Depth ±0.10 m

Table B.1. Bathymetric Survey Data

Easting	Northing	Depth	Easting	Northing	Depth
73.978	-155.792	97.380	24.352	255.706	95.950
83.682	-159.944	97.290	46.091	198.282	98.330
74.837	-173.882	97.280	73.313	195.598	97.430
51.904	-175.526	97.770	61.663	189.420	98.330
67.600	-188.568	97.490	103.093	176.576	98.430
52.917	-189.530	97.700	102.185	176.357	97.330
62.048	-198.532	97.600	68.803	141.842	98.550
38.976	-209.853	97.490	106.061	109.219	97.950
52.433	-212.925	97.700	94.475	106.451	97.770
46.319	-222.277	97.710	70.375	100.195	98.400
24.631	-230.826	97.720	38.158	83.925	98.710
32.523	-242.690	97.630	97.130	71.486	97.740
10.252	-251.250	97.830	71.791	70.357	98.330
23.030	-257.854	97.730	108.599	66.895	97.950
-5.548	-274.050	98.050	72.194	56.004	98.260
-36.373	-283.112	99.050	110.704	52.939	97.780
7.037	-293.031	98.260	44.402	47.992	98.780
-48.190	-300.445	99.060	110.879	39.919	97.990
6.163	-306.058	98.470	72.889	33.288	98.190
-28.412	-308.290	98.080	91.736	30.583	97.900
-8.746	-315.124	98.390	111.303	27.013	97.900
-59.606	-318.329	98.890	48.891	23.733	98.700
-40.688	-324.490	98.210	110.266	15.443	97.810
-67.088	-328.172	99.010	83.289	11.052	97.800
-9.579	-332.140	99.030	77.380	5.639	97.920
-26.627	-339.754	98.340	110.531	4.823	99.070
-79.252	-340.357	99.040	110.802	-7.497	97.640
-17.740	-342.083	98.750	110.788	-25.967	97.460
-58.133	-347.869	98.370	109.876	-29.893	97.450
-91.735	-355.607	99.080	48.941	-31.118	98.840
-30.820	-358.114	98.680	79.217	-31.291	97.250
-42.246	-361.471	98.290	110.833	-42.211	97.660
-96.042	-370.192	99.000	111.453	-48.527	97.460
-43.317	-375.239	99.120	58.811	-61.537	98.650
-58.545	-384.636	98.420	103.893	-63.743	96.260
-84.139	-385.435	98.630	70.939	-73.645	97.470
-100.706	-386.769	98.930	72.449	-95.688	97.070
-51.358	-388.347	99.120	95.573	-103.198	96.070
-65.543	-411.398	99.140	90.556	-119.684	96.280
-80.112	-416.914	98.550	44.996	-126.499	98.880
39.474	191.450	98.729	62.507	-152.398	97.590

Table B.1. Continued

Easting	Northing	Depth
60.089	187.251	98.289
16.859	52.530	99.212
37.846	51.123	98.578
42.931	29.840	98.598
47.939	4.067	98.556
36.717	-15.795	99.289
49.884	-21.460	98.596
52.930	-35.171	98.597
36.910	-97.498	99.300
53.782	-99.570	98.589
26.381	-157.036	99.324
27.462	-163.626	98.597
71.800	215.100	99.112
89.000	201.800	99.180
99.300	187.300	99.232
104.200	172.100	99.251
105.800	151.100	99.257
111.300	124.600	99.267
120.000	-50.600	99.346
114.500	-88.400	99.358
107.700	-117.800	99.362
89.900	-162.100	99.363
76.700	-188.600	99.365
60.200	-212.800	99.367
19.200	-282.900	99.399
35.100	136.600	98.590
3.800	138.600	98.860
33.100	155.500	98.670
36.100	111.200	98.650
68.400	121.200	98.480
63.900	163.400	98.420
36.100	174.300	98.700
16.700	211.100	98.550
50.640	138.380	98.556
42.620	63.130	98.600
21.020	126.010	98.757
24.200	97.850	98.796
10.010	155.860	98.800
51.720	68.000	98.500
29.700	58.690	98.800
47.230	169.360	98.500
49.800	97.630	98.500
13.580	144.360	98.798
6.810	170.530	98.790
15.690	132.910	98.800
28.300	67.490	98.790
31.340	43.660	98.790
34.850	18.200	98.800
50.250	123.600	98.500
48.850	152.060	98.500
49.790	111.000	98.500
47.690	160.220	98.500
98.438	153.158	97.640
101.228	138.940	97.660
104.293	120.120	97.830
107.209	91.428	97.910
108.046	82.195	97.930

Appendix C: Seismic Survey

C.1. Seismic Survey

A seismic survey was performed in order to elucidate the depth and structure of alluvium at the site. The 2 seismic surveys were performed on the site. The first was oriented approximately along the longitudinal centerline of the gravel bar. The second was positioned at the midpoint of the centerline and was oriented orthogonally to the first. Both surveys consisted of a 60 geophone array spaced at a 2 m interval along the survey strike line. Our signal source was generated by striking a steel plate that had coupled to the ground. Coupling was accomplished by excavating a shallow hole (30 cm X 30 cm 10 cm) filling with wetted sand. The result of a preliminary model is presented here. The model and comments were provided by Dr. A. T. Trehu (Figure C.1.).

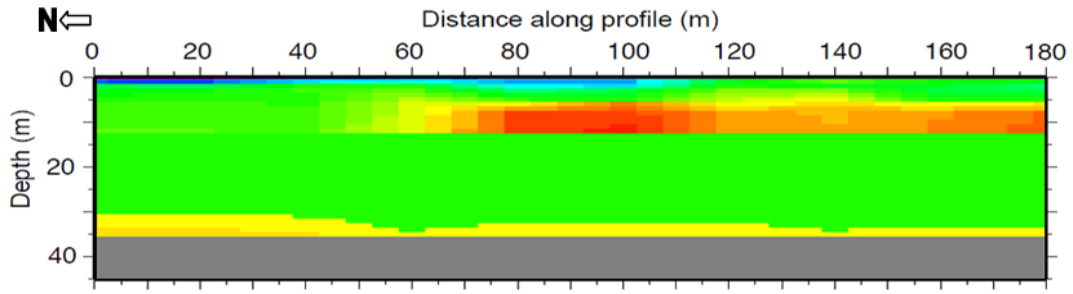

Figure C.1 Seismic Survey Model

The preliminary model generated from the seismic survey indicates that there are four primary zones of differing structure.1.) Very thin blue zone at the top (velocity ~600 m/s) is the unsaturated zone. It is present only from about 0-100 m and is very thin. 2.) velocities in the upper 12 m vary laterally and go above 2000 m/s in places (and perhaps as high as 2500 m/s). 3.) there is an inversion in velocity, with velocities of 1800-1900 m/s below the shallow region in the upper 12 m. 4.) there is an abrupt increase in velocity at about 30 m depth.

Appendix D: Thermistor Temperature Probes

D.1. Thermistor Temperature Probes

Construction

The thermistor temperature probes consisted of two basic components, the probe casing and a rod to which thermistors (Onset tidbit V2 temperature data loggers[11]) were attached. The probe casings were constructed from 2 m lengths of 7.62 cm diameter schedule 40 PVC pipe. A 3.2 cm X 150 cm slot was cut 50 cm from one end of the casing. The slot enabled the thermistors to be exposed directly substrate.

The rod to which 4 V2 loggers were attached was a 3.8 cm PVC pipe. The loggers were spaced 10 cm apart beginning at the end of the rod. Attached to the PVC rod on the side opposite of the thermistors was a rubber air bladder. When inflated, the thermistors would be pushed to the exterior of the probe casing

Installation

The thermistor temperature probes were oriented in the gravel bar so that they would collect data in a similar fashion to that of the fiber optic DTS system. The probe casings were installed using a modified version of the direct-push method of monitoring well installation for near surface aquifers. The tool used to install the fiber optic probes was also used to install the casings which housed the V2 logger probes. The installation apparatus consisted of a steel sleeve with an inner diameter of 6.35 cm over a solid driving rod. The sleeve and driving rod were driven into the ground simultaneously to the desired depth. The driving rod was then removed from the sleeve. The probe casing was then inserted, and the steel sleeve was removed. The rod to which the V2 loggers were attached was then inserted into the casing where the top logger was just below the water's surface and aligned with the slot of the casing. The air bladder was then inflated to push the face of the loggers into the gravel.

For complete data series, see "Thermistor Data" folder in attached CD

---

[11] Onset Tidbit V2 Temperature Data Loggers [Bourne, MA, USA] - The V2 temperature data loggers have a resolution of 0.02° C and an accuracy of ±0.2° C.

Appendix E: Methods of Hydraulic Conductivity Assessment

E.1 Falling-head Slug Test:

E.1.1. Purpose:

The slug tests were conducted as falling-head tests. Water levels were recorded as the well head recovered to a static level following the addition of a water "slug."

E.1.2. Procedure:

1) A WL16 Water Level Logger (Global Water Instrumentation, Inc., Gold River, California, USA) was placed at the bottom of each piezometer, recording 10 readings per second.
2) Logger recorded static water levels for 1 minute prior to introducing water slug.
3) 1 liter was added to the well.
4) Waited at least 5 minutes for water level to return to initial static water level.
5) Repeated steps 2-4 twice, completing 2 slug tests for each well.

E.1.3. Calculation/Analyses:

For partially-penetrating wells in an unconfined aquifer where recovery curves demonstrated over-dampened behavior, we used the Bouwer and Rice (1976) analytical solution:

$$Kr = \frac{r_c{}^2 \ln(Re/rw)}{2Le} \frac{1}{t} \ln\left[\frac{H0}{Ht}\right]$$

Kr = hydraulic conductivity (L/T)

rc = radius of well casing (L)

rw = radius of gravel envelope (L)

Re = effective radial distance over which head is dissipated (L)

Le = length of the screen

H0 = drawdown at time t = 0 (L)

Ht = drawdown at time t = t (L)

t = time since *Ht* = *H0* (T)

The effective radius parameter, Re, is estimated for a partially penetrating well using the equation:

$$\ln\frac{R_e}{r_w} = \left[\frac{1.1}{\ln(L_w/r_w)} + \frac{A + B\,\ln[(H - L_w)/r_w]}{L_e/r_w}\right]^{-1}$$

A and B are dimensionless numbers determined from Bouwer (1989).

An example applying this method is shown below:

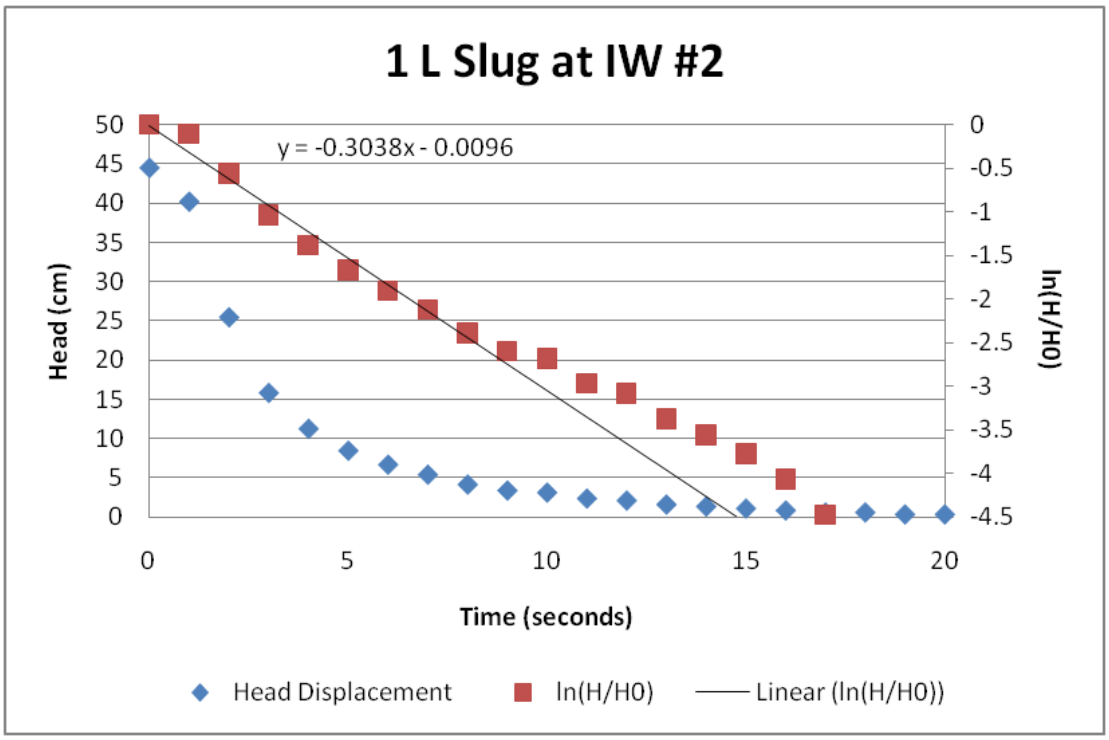

Figure E.1.1 Example of falling head analysis

This plot presents the data collected from IW #2. The blue diamond data points represent the well recovery curve from the time of peak displacement (t_0) to the time of recovery (t). The red squares are the logarithmic derivative of the recovery curve, and black line represents the linear regression of the derivative.

Variables not shown here that were substituted into the analytical solution are: *rc* = radius of well casing (L), *rw* = radius of gravel envelope (L), *Re* = effective radial distance over which head is dissipated (L), *Le* = length of the screen. The solution for this well was found as: *Kr* = 83.78 m/day

E.1.4. Result:

Table E.1.1 Falling head hydraulic conductivity values

Location	Slug	Hydraulic Conductivity K (m/day)
IW 1	Slug 1	328.15
	Slug 2	490.72
IW 2	Slug 1	83.78
	Slug 2	113.51
TW 0	Slug 1	495.26
	Slug 2	560.97
K Well 1	Slug 1	73.67
	Slug 2	N/A
K Well 2	Slug 1	154.15
	Slug 2	138.71

Summary of the slug tests for various locations. Maximum: 560.97 m/day; Minimum: 73.67 m/day; Average: 270.99 m/day. Geometric mean: 206.1 m/day

E.2 Tracer Tests:

Three different tracer tests/analyses were performed in an effort to characterize the hyporheic aquifer. The first was a salt-water injection into the adjacent alcove to ascertain alcove discharge and hydraulic conductivity of the hyporheic zone in the gravel bar. The second was a saltwater injection into the gravel bar to determine hyporheic velocity and direction. The third was an analysis of the diurnal temperature signal advecting through the gravel bar.

E.2.1. Alcove Injection

E.2.1.1. Purpose:

Alcove discharge is the cumulative or "bulk" discharge of hyporheic flow. By determining the alcove area and discharge, we can apply the one-dimensional form of Darcy's Law to estimate the bulk hydraulic conductivity of the hyporheic zone in the gravel bar.

E.2.1.2. Procedure:

E.2.1.2.1. Alcove Area

1) The alcove shoreline was mapped using a total station. By converting the survey data points into a triangular irregular network (TIN), the area for the polygon was calculated using geographic information system software.

E.2.1.2.2. Saltwater Tracer

1) Background specific conductivity measurements were taken prior to experimental setup using a YSI 63 electrical conductivity and temperature probe (Yellow Springs, Ohio, USA); 68.3 µs/cm @ 28.1 °C.

2) The saltwater solution was prepared in a 60 L carboy. Specific Conductivity = 75550.0 µs/cm @ 27.3 °C.

3) The saltwater solution was then injected into the alcove at the injection point indicated on the inset map of Figure F.2.1.1. The pumping rate was 1.7 L/min.

Concurrent to the injection of the saltwater, electrical conductivity (EC) was monitored at location S3 (see Figure F.2.1.2).

4) Measurements continued on an approximate 15 minute interval until a peak concentration was apparent, at which point, measurements ceased.

E.2.1.3. Calculation/Analysis and Result:

E.2.1.3.1. Alcove area

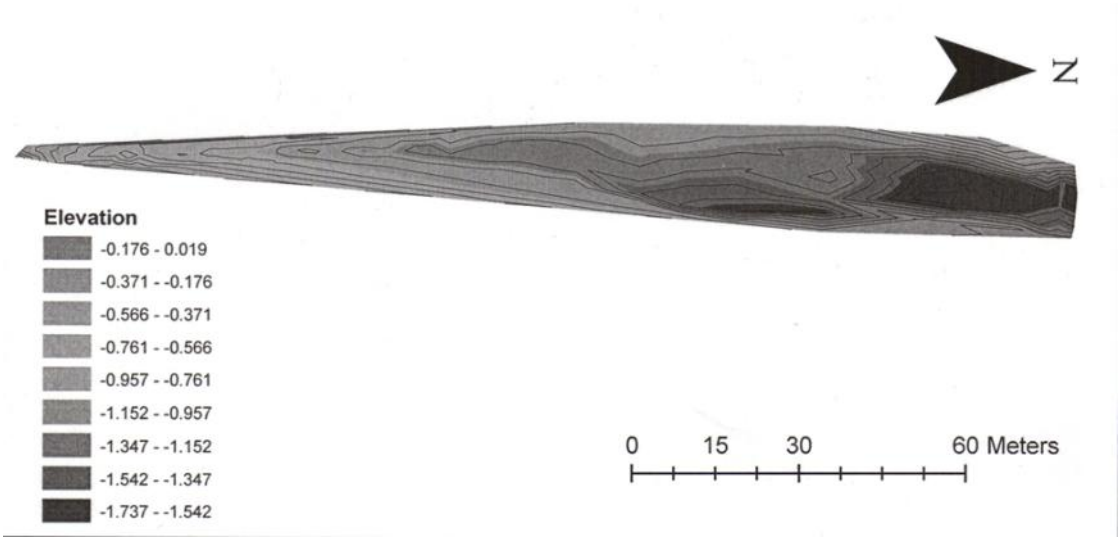

Figure E.2.1.1 Alcove Area

A triangulated irregular network (TIN) map was generated using geographic information system (GIS) software and the survey data delineating the alcove. The alcove surface area was calculated to be 4590 m^2. Elevations are relative to arbitrary baseline datum.

E.2.1.3.2. Saltwater Injection

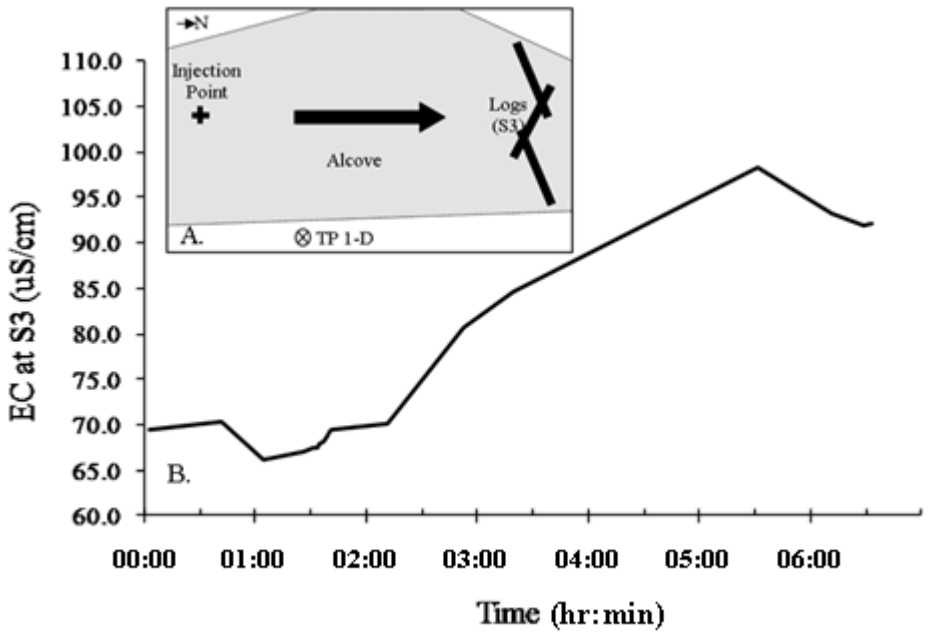

Figure E.2.1.2 Alcove Breakthrough Curve

Site description (A.) and the breakthrough curve of the saltwater injection into the alcove (B.).

E.2.1.3.1. Alcove Discharge Calculation:

$$Q = P * \left(\frac{EC_{carboy} - EC_{peak}}{EC_{peak} - EC_{background}}\right) \quad \text{(E.1)}$$

Where:

Q = Alcove discharge.

EC_{carboy} = Electrical conductivity of the carboy.

EC_{peak} = maximum electrical conductivity of the breakthrough curve.

$EC_{background}$ = Background electrical conductivity of the alcove.

P = pumping rate of the injection.

For:

EC_{carboy} = 75550.0 µs/cm

EC_{peak} = 98.4 µs/cm

$EC_{background}$ = 68.3 µs/cm

P = 0.00271 L/sec

Q = 6.8 L/sec

E.2.1.3.2. Hydraulic Conductivity Calculation:

1-D form of Darcy's Law:

$$Q = A * k * \nabla H \quad \text{(E.2)}$$

Solved for k:

$$k = \frac{Q}{A*\nabla H} \quad \text{(E.3)}$$

Where:

k = Hydraulic conductivity.

Q = Alcove discharge.

A = Wetted alcove area.

h_{river} = The average elevation of the water's surface at the shoreline. Shoreline length incorporated was ±10 m upstream and downstream of the instrumentation.

h_{alcove} = Average elevation of water's surface in the alcove.

L_{HZ} = Length of the hyporheic zone (width of the gravel bar.)

For:

Q = 6.8 L/sec = 0.0068 m^3/sec

A = 4590 m^2

$$\nabla H = \frac{h_{river} - h_{alcove}}{L_{HZ}} = \frac{99.264\ m - 98.861\ m}{82.416\ m} = 0.00489$$

k = 3.03* 10^{-4} m/sec = 26.1 m/day

E.2.2. Bar Injection

E.2.2.1. Purpose:

In an effort to observe the pore velocity and direction of the hyporheic flow in the gravel bar, a saltwater injection was performed.

E.2.2.2. Procedure:

1) Piezometers were installed on the gravel bar in the area where temperature measurements were to take place. The piezometers were constructed from 0.032 m PVC pipes, and were installed using a modified form of the direct push method. The method is similar to that used to install the fiber optic and thermistor temperature probes.

2) A Campbell Scientific Logger with multiplexor was configured to log multiple electrical conductivity (EC) sensors simultaneously. The sensors were deployed in the piezometers as well as locations that were identified as preferential hyporheic pathways (Figure E.2.2.1..; unlabeled circles). The YSI 63 EC and temperature sensor was used to verify the Campbell Scientific logger's readings. The logger was programmed to record a measurement on a 1 minute interval.

3) A 200 ppm saltwater solution was prepared in a 60 L carboy.

4) The saltwater solution was pumped into IW #1 (Figure E.2.2.1.) at a rate of 1.7 L/min.

5) Breakthrough was monitored until the unit lost power.

E.2.2.3. Calculation/Analysis and Result:

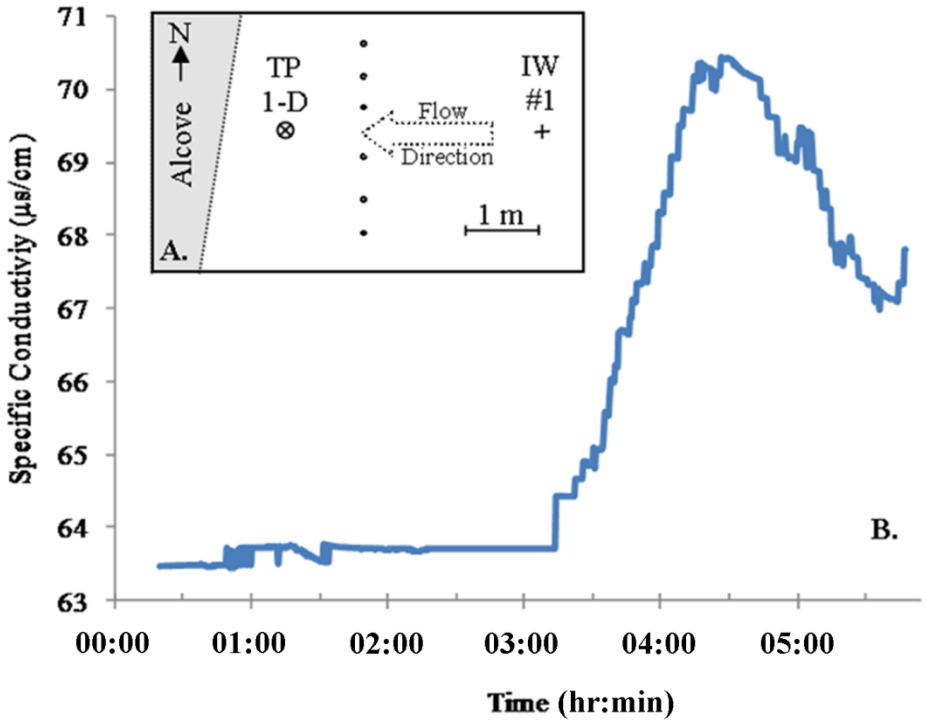

Figure E.2.2.1 Gravel bar breakthrough curve

Site description (A) and gravel bar breakthrough (B). Arrival of breakthrough at TP 1-D indicates an average linear hyporheic velocity of 66 m/day.

Appendix F: Numerical Groundwater Model

F.1. Groundwater Model

F.1.1. Purpose:

A three-dimensional, steady-state ground water flow model was created to simulate hyporheic flow through the gravel bar. The flow model was developed via the Groundwater Modeling Systems (GMS) 6.0 software platform, utilizing the MODFLOW (USGS, 2000) and MODPATH modules.

F.1.2. Procedure:

F.1.2.1. The Conceptual Model:

Using survey, piezometer, and aerial photography data, a 40 layer finite-difference grid was created using the conceptual model approach. The grid size ranged from 0.20 m X 0.20 m X 0.20 m (X, Y, and Z planes respectively) in the area of the instrumentation to 5 m X 5 m X 2 m at the outer boundary. The outer boundary condition was set as a no flux boundary. River stage elevation was characterized as a specified head boundary condition. The model was calibrated by adjusting hydraulic conductivity zones so that water table elevations matched observed elevations in the piezometer array. Once a successful MODFLOW simulation was generated, The MODPATH module in GMS was used to simulate hyporheic flow paths and determine flow geometry through the bar.

For complete computer model, see "Groundwater Flow Model" folder in attached CD.

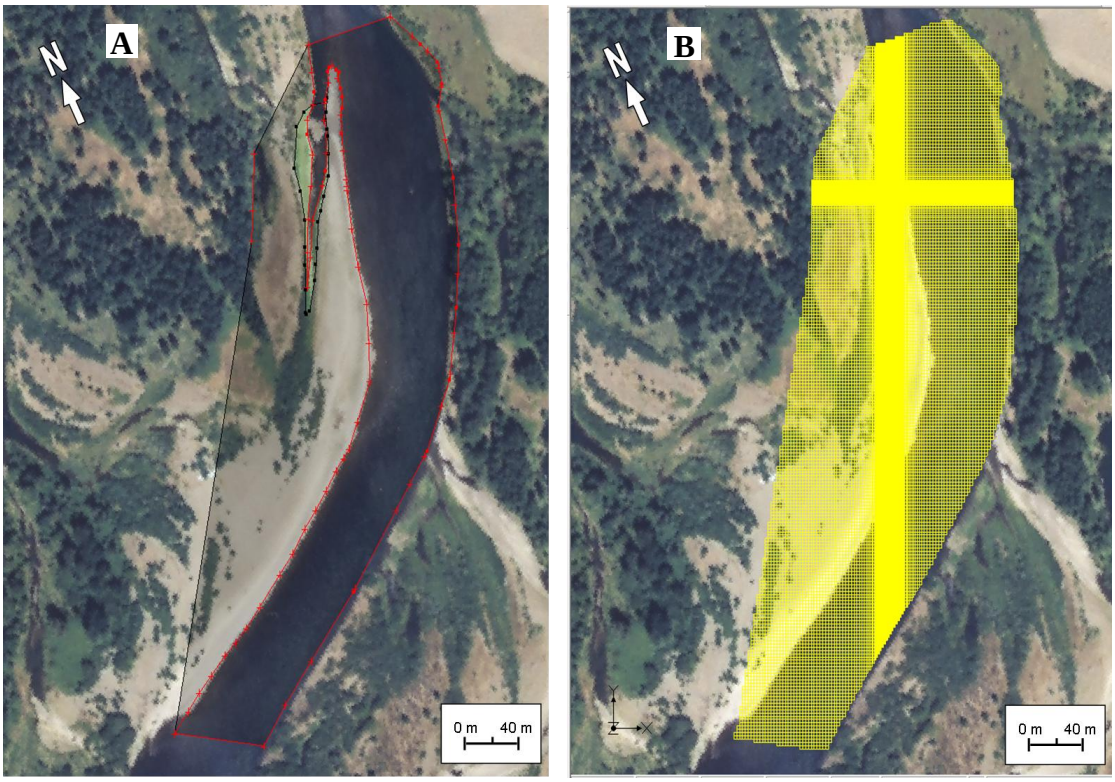

Figure F.1.1 Flow Model Domain and Grid

The model domain encompassed the majority of the newer exposed gravel bar. “A” (left) illustrates the boundary conditions of the model domain (red- specified head condition). “B” (right) illustrates the areas of grid refinement for the model domain and the area surrounding the instrumentation.

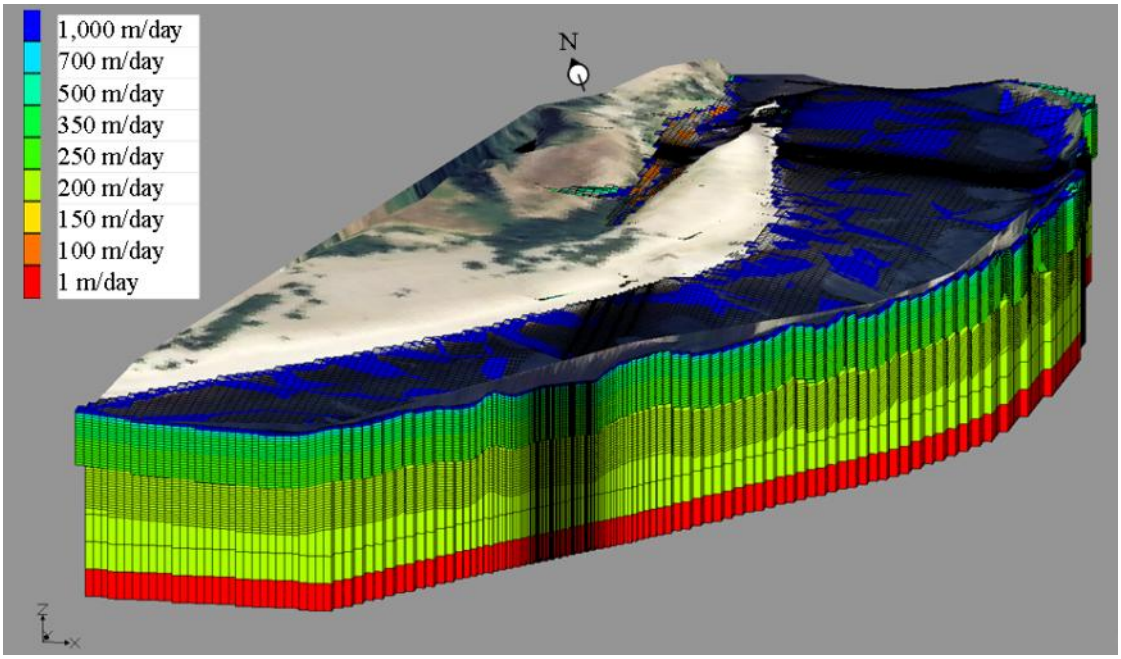

Figure F.1.2 3–Dimensional grid and horizontal hydraulic conductivity values

The hydraulic conductivity of the top layers was determined via the results of the falling head test. The bottom layer was arbitrarily set to a lower hydraulic conductivity than the surface in order to simulate bottom of the alluvial aquifer. Hydraulic conductivities > 2 m depth were based on a linear interpolation of values between second and bottom layers.

F.1.3. Result:

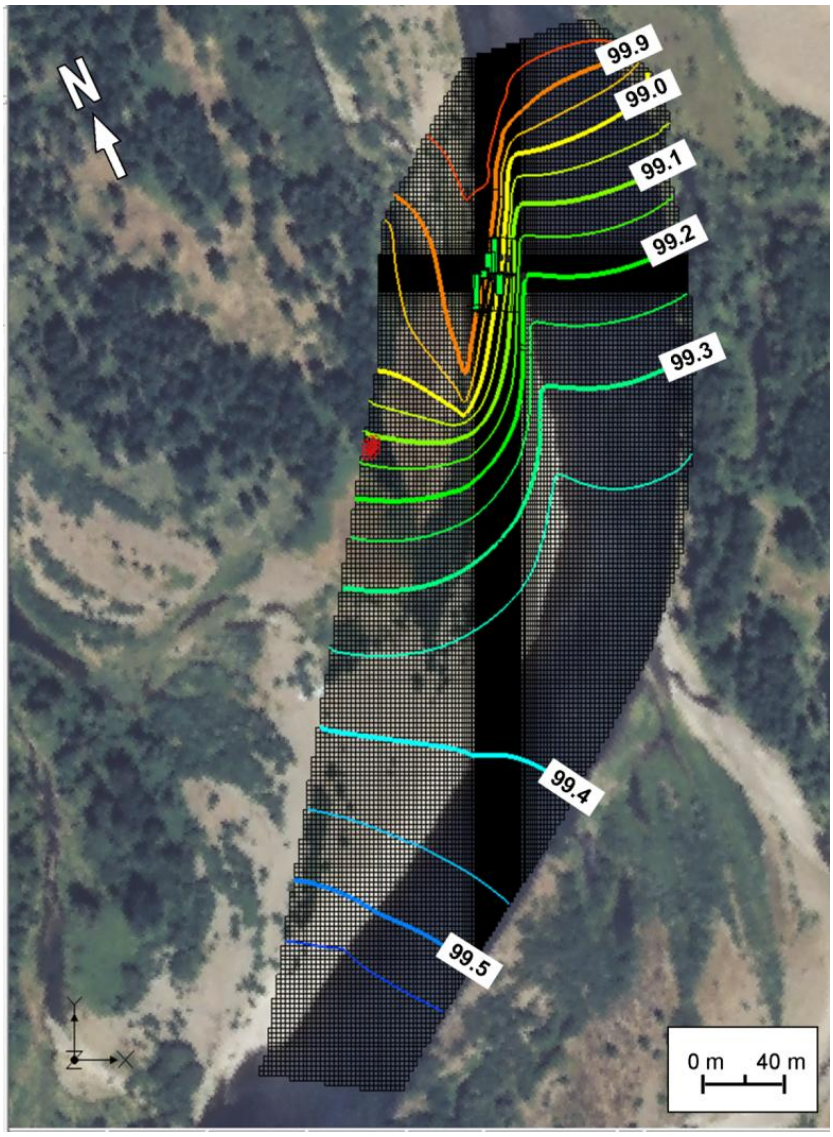

Figure F.1.3 Potentiometric Map.

The result of the MODFLOW simulation. Contour elevation is relative to an arbitrary benchmark elevation of 100 m. Calibration targets (green bars at center of figure) represent water surface elevation in selected piezometers in the instrumentation array.

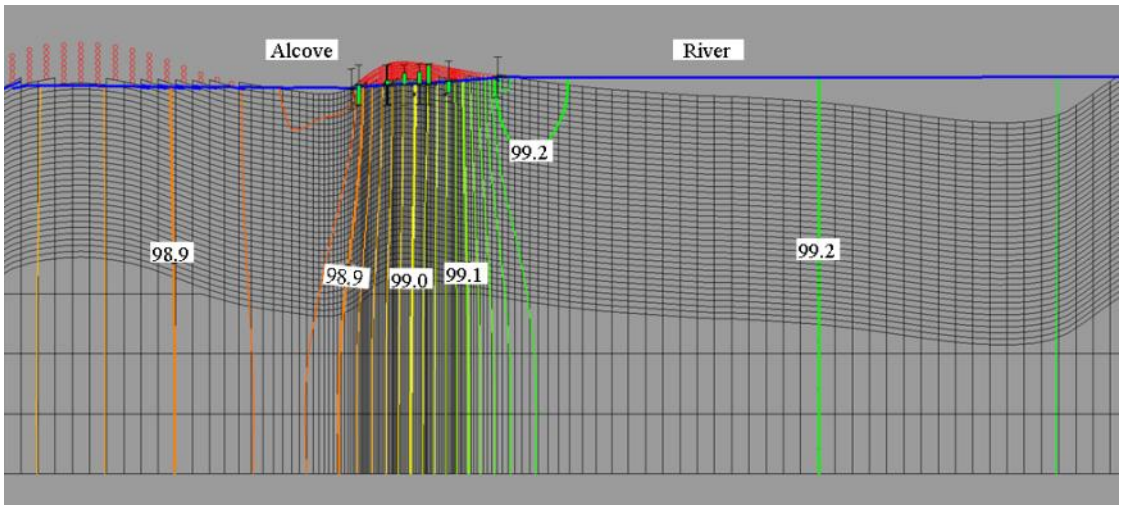

Figure F.1.4 Cross–sectional view

This is a cross–sectional view of the GMS model facing north. Elevations are expressed meters and are arbitrarily relative to 100 m. The heavy blue line denotes the elevation of the water table.

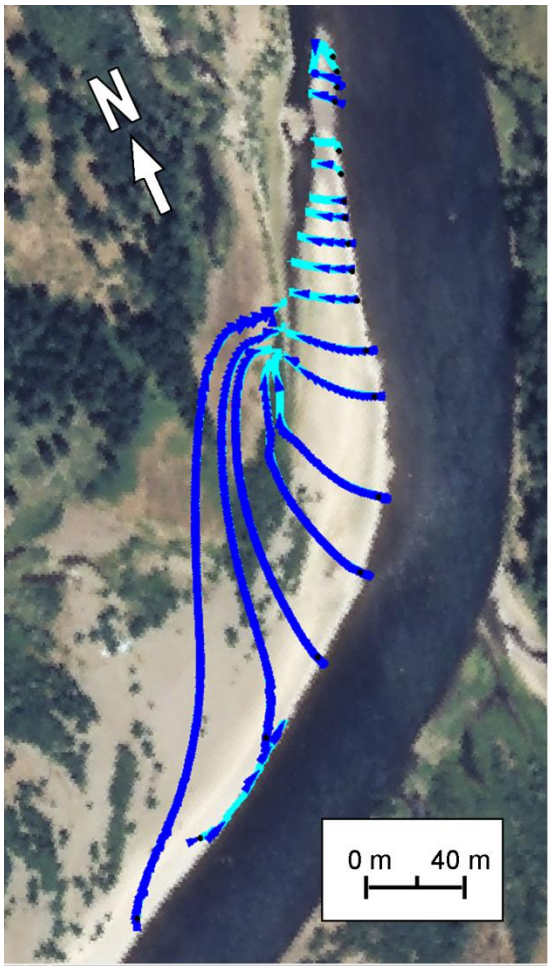

Figure F.1.5 Hyporheic Flow Paths.

Hyporheic flow direction was simulated using the MODPATH module within GMS.

Appendix G: Numerical Heat Transport Model

G.1. Heat Model

G.1.1. Purpose:

A two-dimensional finite element transient heat transport model was created using HYDRUS 3D [*Šimůnek et al.*, 2005]. The domain dimensions of the heat transport model were taken from a cross-sectional slice of the GMS groundwater model at the location of the instrumentation (Figure F.1.4.).

G.1.2. Procedure:

G.1.2.1 The Conceptual Model:

Using survey, piezometer, and GMS MODFLOW simulations a finite-element grid was created using the conceptual model approach. The grid size ranged from 1 m to 0.1 m, grid was refined in the region from the water table to the depth of sensor penetration. The hydraulic boundaries were established at both alcove and river topographical minima. River stage elevation was characterized as a constant head boundary condition and the hydraulic conductivity was obtained from the calibrated GMS model. Once a complete HYDRUS model was calibrated, transport of the diurnal temperature fluxuations was used to estimate thermal properties (XYZ) of the gravel bar materials.

For complete computer model, see "Heat Transport Model" folder in attached CD.

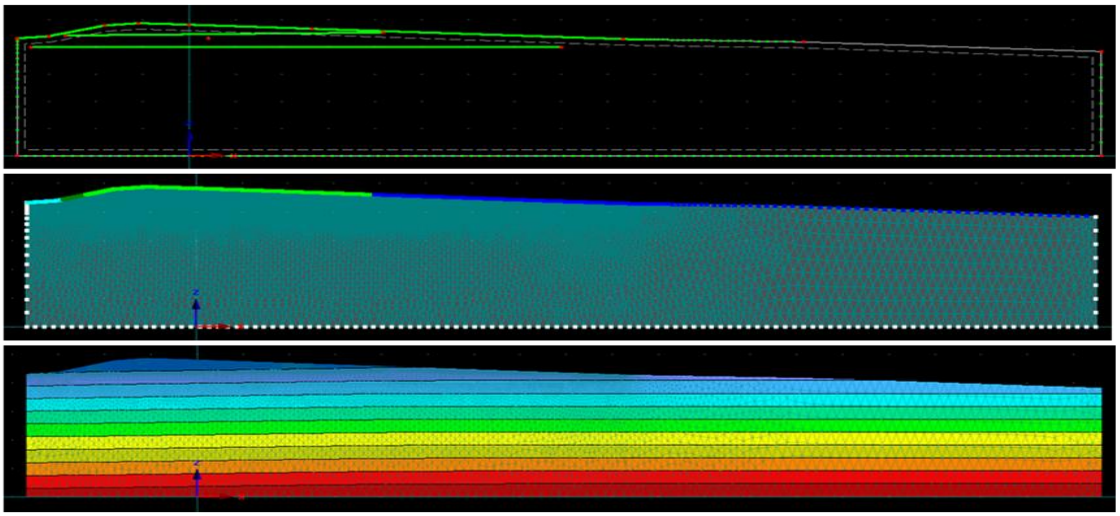

Figure G.1.1 HYDRUS Model Domain, Grid and Initial condition

A 0.5 stretching factor has been applied to the horizontal distances in the above graphics. The model domain was designed using the GMS cross–section in Figure F.1.4. Based on the result of the 3–D model, it was determined that the left and right bounds of the 2–dimensional model were the hydraulic minimums for the alcove and river. Element spacing was refined to 0.2 m in the area of the water table, while universal spacing approached 1 m. The left and right boundaries were considered no–flux boundaries. The bottom boundary of the domain was also a no–flux condition. The alcove boundary was defined as a constant pressure head. A seepage face boundary condition was applied from the maximum elevation of the alcove to an elevation equal to the river. An atmospheric boundary condition was applied to the gravel bar's surface. The river was given a variable boundary condition. The pressure head was held constant throughout the simulation, while the temperature was varied according to field measurements. The initial pressure head condition was established using elevation data derived from the GMS model.

G.1.3. Result:

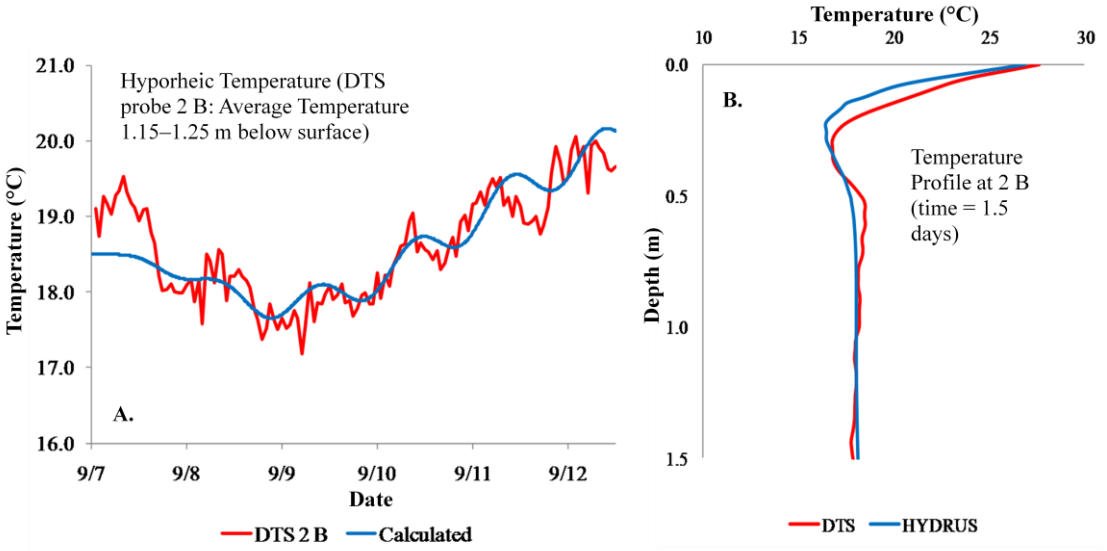

Figure G.1.2 HYDRUS Simulation – Observed vs. Calculated

Plot A (at left) presents the fit of the model simulation to a section of probe 2 B for the duration of the sampling period. Plot B (at right) presents the fit of the model simulation to the vertical temperature profile of probe 2 B at one time (1.5 days).